



ALMA MATER STUDIORUM  
UNIVERSITÀ DI BOLOGNA

ARCHIVIO ISTITUZIONALE  
DELLA RICERCA

## Alma Mater Studiorum Università di Bologna Archivio istituzionale della ricerca

Sedimentological analysis of ash-rich pyroclastic density currents, with special emphasis on sin-depositional erosion and clast incorporation: The Brown Tuff eruptions (Vulcano, Italy)

This is the final peer-reviewed author's accepted manuscript (postprint) of the following publication:

*Published Version:*

Sedimentological analysis of ash-rich pyroclastic density currents, with special emphasis on sin-depositional erosion and clast incorporation: The Brown Tuff eruptions (Vulcano, Italy) / Lucchi, F.; Sulpizio, R.; Meschiari, S.; Tranne, C.A.; Albert, P.G.; Mele, D.; Dellino, P.. - In: SEDIMENTARY GEOLOGY. - ISSN 0037-0738. - STAMPA. - 427:(2022), pp. 106040.1-106040.23. [10.1016/j.sedgeo.2021.106040]

*Availability:*

This version is available at: <https://hdl.handle.net/11585/849294> since: 2022-11-22

*Published:*

DOI: <http://doi.org/10.1016/j.sedgeo.2021.106040>

*Terms of use:*

Some rights reserved. The terms and conditions for the reuse of this version of the manuscript are specified in the publishing policy. For all terms of use and more information see the publisher's website.

This item was downloaded from IRIS Università di Bologna (<https://cris.unibo.it/>).  
When citing, please refer to the published version.

(Article begins on next page)

This is the final peer-reviewed accepted manuscript of:

**F. Lucchi, R. Sulpizio, S. Meschiari, C.A. Tranne, P.G. Albert, D. Mele, P. Dellino, Sedimentological analysis of ash-rich pyroclastic density currents, with special emphasis on sin-depositional erosion and clast incorporation: The Brown Tuff eruptions (Vulcano, Italy), *Sedimentary Geology*, Volume 427, 2022, 106040**

The final published version is available online at <https://dx.doi.org/10.1016/j.sedgeo.2021.106040>

Terms of use:

Some rights reserved. The terms and conditions for the reuse of this version of the manuscript are specified in the publishing policy. For all terms of use and more information see the publisher's website.

*This item was downloaded from IRIS Università di Bologna (<https://cris.unibo.it/>)*

***When citing, please refer to the published version.***

1 **Sedimentological analysis of ash-rich pyroclastic density currents, with special emphasis on sin-**  
2 **depositional erosion and clast incorporation: the Brown Tuff eruptions (Vulcano, Italy)**

3

4 F. Lucchi <sup>a,\*</sup>, R. Sulpizio <sup>b,c,d</sup>, S. Meschiari <sup>a</sup>, C.A. Tranne <sup>a</sup>, P.G. Albert <sup>e,f</sup>, D. Mele <sup>b</sup>, P. Dellino <sup>b</sup>

5

6 <sup>a</sup> Dipartimento di Scienze Biologiche, Geologiche e Ambientali, Università di Bologna, Piazza Porta  
7 S. Donato 1, 40126 Bologna, Italy

8 <sup>b</sup> Dipartimento di Scienze della Terra e Geoambientali, Università di Bari, via Orabona 4, 70125 Bari,  
9 Italy

10 <sup>c</sup> INGV- Bologna section, via D. Creti, 40100, Bologna, Italy

11 <sup>d</sup> IGAG-CNR, Area della Ricerca di Roma 1- Strada Provinciale 35d, Montelibretti (Rome), Italy

12 <sup>e</sup> Department of Geography, Swansea University, Singleton Park, Swansea SA2 8PP, UK

13 <sup>f</sup> Research Laboratory for Archaeology and the History of Art (RLAHA), University of Oxford,  
14 Dyson Perrins Building, South Parks Road, Oxford OX1 3QY, UK

15

16 \* Corresponding author

17

18 **ABSTRACT**

19 The sedimentological, lithological and textural characteristics of the Brown Tuffs (BT) pyroclastic  
20 deposits, combined with their grain-size, componentry and geochemical glass compositions, are here  
21 investigated to obtain information on the transport and depositional mechanisms of the corresponding  
22 pyroclastic density currents (PDCs). The BT are widespread reddish-brown to grey, ash-rich  
23 pyroclastic deposits generated by pulsating hydromagmatic explosive activity from the La Fossa  
24 Caldera on Vulcano island during the c. 80-6 ka time-stratigraphic interval, and then distributed on  
25 most of the Aeolian Islands and Capo Milazzo peninsula (Sicily) and in the Tyrrhenian and Adriatic  
26 Sea regions. Near the source area on Vulcano, the BT are characterised by alternating massive and

|

27 planar to cross stratified lithofacies that result from the stepwise, repeating aggradation of discrete  
28 PDC pulses. This alternance is regulated by either fluid escape or granular flow depositional regimes  
29 at high clast concentration or grain by grain traction deposition in the waning diluted stages of the  
30 PDCs. Most of the BT on Vulcano show intermittently stratified and massive ash deposits resulting  
31 from a pervasive post-depositional disruption of the primary structures. This is induced by upward  
32 fluid expulsion associated with dissipation of pore pressure between layers at different grain size (fine  
33 to coarse ash) and porosity, as outlined by distinctive upwards bends and pillar-type escape structures  
34 through the fluid-filled cracks and rupture points. Massive BT deposits with a faint colour and grain-  
35 size banding are widely recognised on Lipari, the nearby island of Vulcano. Based on the presence,  
36 at the base of BT depositional units, of cm-thick amalgamation bands containing pumice lapilli, scoria  
37 and lithic clasts ripped-up and embedded from the loose underlying pyroclastic units, they are  
38 interpreted as deposited by ash-rich PDCs laterally spreading from La Fossa Caldera and moving to  
39 Lipari. During their motion to Lipari these currents (likely) crossed a narrow and shallow sea-water  
40 inlet which did not stop their advancement but influenced the grain size distribution of those spreading  
41 on the Lipari mainland. In this paper, the mechanism of clast erosion and incorporation is outlined  
42 across the whole island of Lipari by means of field study, grain-size, and geochemical glass analyses  
43 on the different components of the mixed basal bands of the BT. This suggests that the BT PDCs  
44 maintained enough flow power as to erode the substratum, hence likely impacting the territory, over  
45 a distance up to at least 16-17 km from the volcanic source. Evidence that the BT PDCs exerted a  
46 high shear-stress over the loose substratum is also provided by undulated, recumbent flame and rip-  
47 up structures at the base of some depositional units in southern and central Lipari. In order to form  
48 such bed granular instabilities between the BT and the underlying deposits we calculate that the  
49 currents had at least a shear velocity of ca.  $2 \text{ m s}^{-1}$  and a shear stress in the range of 1-4.5 kPa. These  
50 results add new insights on the large-scale hazard at the Aeolian Islands and shed new lights on the  
51 widespread transport and depositional dynamics of ash flows spreading over the sea and reaching  
52 nearby islands, and their interactions with the substratum and the pre-depositional topography.

53

54 **KEYWORDS**

55 Brown Tuffs, Aeolian Islands, Sedimentary structures, Pyroclastic density current, Clast embedding,  
56 Shear-related granular instability structures

57

58 **1. INTRODUCTION**

59

60 Pyroclastic density currents (PDCs) are ground hugging mixtures of particles and gas that  
61 flow laterally across the topography, and are among the most amazing, complex and dangerous  
62 volcanic phenomena (e.g., Carey, 1991; Druitt, 1998; Branney and Kokelaar, 2002; Sulpizio et al.,  
63 2014; Lube et al., 2020). Irrespective whether they are concentrated or diluted, PDCs are  
64 characterised by a very hostile nature and a complex interplay between transport and depositional  
65 mechanisms, which make their study a great challenge for volcanologists. The only way we have to  
66 get information about the processes occurring at the time of deposition is to analyse the deposit  
67 lithofacies and lithofacies associations in the field (e.g., Sohn and Chough, 1989; Branney and  
68 Kokelaar, 2002; Sulpizio et al., 2008a, 2010) or to replicate PDCs in the laboratory (Dellino et al.,  
69 2007; 2010; Andrews and Manga, 2012; Sulpizio et al., 2016; Breard and Lube, 2017; Brosch and  
70 Lube, 2020). This is particularly demanding for ash rich PDCs that usually have a massive structure  
71 and homogeneous lithology, which make a unique sedimentological interpretation challenging.  
72 Furthermore, quite rare is in the volcanological literature the analysis of the interaction between  
73 PDCs and the pre-depositional topography, which can influence the runout and the internal  
74 organisation of the parent currents by means of the bulking due to substratum erosion (Roche et al.,  
75 2013; Bernard et al., 2014; Roche, 2015; Pollock et al., 2019).

76 The Brown Tuffs (BT) deposits, largely outcropping over the Aeolian islands and northern  
77 Sicily (Italy), represent an exceptional case-study for shedding light on the elusive processes that  
78 drive erosion and deposition in ash-rich PDCs, and their interactions with the substratum. The BT

|

79 are ash-rich, reddish-brown to grey volcanoclastic deposits from PDCs and associated fallout  
80 produced over a long-time span by pulsating hydromagmatic eruptions from the La Fossa Caldera  
81 on Vulcano island (Lucchi et al., 2008, 2013b; Cicchino et al., 2011; Meschiari et al., 2020). They  
82 usually crop out as massive, moderately to well sorted, fine to coarse ash deposits of meter-scale  
83 thickness. Their quite ubiquitous massive appearance, recurring over a wide time span in the  
84 stratigraphy of the Aeolian Islands, and the paucity of distinctive sedimentological characteristics  
85 have long made it difficult to define the eruptive and depositional mechanisms of the BT. As such,  
86 they have been generically interpreted either as primary deposits from PDCs or fallout, reworked  
87 deposits from wind-blown volcanic ash (tuff-loess) or even paleo soils (Bergeat, 1899; Keller, 1967,  
88 1980a, 1980b; Pichler, 1980; Crisci et al., 1981, 1983, 1991; Manetti et al., 1988, 1995; Morche,  
89 1988; Losito, 1989; Gioncada et al., 2003). According to the most accepted interpretation, they  
90 were emplaced on Vulcano and southern Lipari islands by mostly dilute PDCs, based on the  
91 occurrence of rare stratified lithofacies, internal colour and grain-size banding (fine to coarse ash)  
92 and topography-controlled thickness variations (De Astis et al, 1997; Lucchi et al., 2008, 2013b;  
93 Dellino et al., 2011; De Rosa et al., 2016), although more detailed information on the transport and  
94 depositional behaviour of these PDCs has been missing so far. BT deposits cropping out in more  
95 distal outcrops on the other islands of the Aeolian archipelago and the Capo Milazzo peninsula were  
96 instead related to fallout from a pulsating eruption columns or co-ignimbrite ash clouds (Lucchi et  
97 al., 2008).

98         We present here an in-depth field study of the lithological and sedimentological  
99 characteristics of the BT in the proximal and medial-distal outcrops on Vulcano and Lipari islands  
100 (Fig. 1A), with the aim of investigating in detail the transport and depositional mechanisms of the  
101 corresponding PDCs. Special attention was paid to the evidence of erosion and clast incorporation  
102 in the basal portions of some BT depositional units, which were previously signalled by Lucchi et  
103 al. (2008; 2013b). Together with the occurrence of shear-related sin-depositional sedimentary  
104 structures, this can provide information about the processes occurring in the basal portion of PDCs,

105 which transport the vast majority of the total flow mass (Branney and Kokelaar, 2002; Sulpizio et  
106 al., 2014) and determine the threat of these dangerous phenomena (Sulpizio et al., 2014; Dufek et  
107 al., 2015; Pollock et al., 2019). In recent times, the erosive capacity of PDCs and their ability to  
108 produce sin-depositional substrate deformation by shear forces was studied by means of  
109 observations in the field (e.g. LaBerge et al., 2006; Cas et al., 2011; Pollock et al., 2019; Doulliet et  
110 al., 2019) or small scale laboratory experiments (e.g. Roche et al., 2013), mostly focused on  
111 polydisperse, poorly sorted, concentrated PDC deposits (e.g. those related to the 1980 Mt. St.  
112 Helens eruption; Pollock et al., 2019). Nothing has been done, however, on the erosive capability of  
113 well sorted, ash rich PDCs. In order to contribute to bridging this gap, we carried out a detail field  
114 investigation of the lower portions of the ash-rich BT depositional units supported by grain-size,  
115 componentry and geochemical analyses, which helped in deciphering the depositional dynamics of  
116 BT PDCs and shed new light on the dispersal dynamics of ash-rich PDCs.

117

## 118 **2. GEOLOGICAL SETTING**

119

### 120 **2.1. Aeolian Islands**

121 The Aeolian Islands (Alicudi, Filicudi, Salina, Lipari, Vulcano, Panarea and Stromboli; Fig.  
122 1B) are the emerged portions of an active volcanic system in the Southern Tyrrhenian Sea, which also  
123 includes several seamounts (Barberi et al., 1973; Beccaluva et al., 1985; De Astis et al., 2003;  
124 Chiarabba et al., 2008; Ventura, 2013). Aeolian volcanism entirely occurred during the Quaternary,  
125 as demonstrated by the oldest radiometric age of c. 1.3 Ma of submarine lavas from the Sisifo  
126 seamount (Beccaluva et al., 1985), and then developed subaerially from ~270-250 ka to historical and  
127 present times (Leocat, 2011; Lucchi et al., 2013b, and references therein) (Fig. 1C). Successive  
128 eruptive epochs of the different volcanic islands have been subdivided by volcanic collapses or major  
129 quiescent (erosional) stages (De Astis et al., 2013; Forni et al., 2013; Francalanci et al., 2013; Lucchi  
130 et al., 2013a, 2013c, 2013d, 2013e), sometimes associated with episodes of marine ingression and

131 terrace formation during the major sea-level fluctuations (Lucchi, 2009). The marine terraces  
132 attributed to the marine (oxygen) isotope stage (MIS) 5, dated between c. 124 and 80 ka (Chappell  
133 and Shackleton, 1986; Waelbroeck et al., 2002; Rohling et al., 2014), are well constrained time-  
134 stratigraphic markers on most of the archipelago. The erupted magmas in the Aeolian Islands range  
135 from basaltic andesites to rhyolites over a large range of differing magmatic suites from calc-alkaline  
136 (CA), high-K calc-alkaline (HKCA), shoshonitic (SHO) and K-Series (KS) (Ellam et al., 1988;  
137 Francalanci et al., 1993; Peccerillo et al., 2013). Major Violent Strombolian to Sub-Plinian eruptions  
138 involving dacite to rhyolite magmas have occurred on Lipari, Vulcano, Salina and Stromboli during  
139 the last glacial period (from c. 80 ka) and the early Middle Ages (Crisci et al., 1981; Hornig-  
140 Kjarsgaard et al., 1993; Keller and Morche, 1993; Colella and Hiscott, 1997; De Astis et al., 1997a,  
141 2006). This is the time-stratigraphic period when the BT, the object of the present study, were erupted.

142

## 143 **2.2. The Brown Tuffs**

144 The BT are widespread, reddish-brown to grey, massive ash-rich volcanoclastic deposits with  
145 metric thickness recognised in the Aeolian Islands and the Capo Milazzo peninsula (Sicily).

146 Chemo-stratigraphic and tephrochronological studies by Lucchi et al. (2008, 2013b) and  
147 Meschiari et al. (2020) have documented the BT occurrence, with variable volumes and dispersal  
148 areas, on the islands of Vulcano, Lipari, Salina, Filicudi, Stromboli and Alicudi and the Capo Milazzo  
149 peninsula, and in Tyrrhenian and Adriatic Sea marine cores, in the c. 80-6 ka time-stratigraphic  
150 interval. The BT have been interpreted as the result of PDCs and associated distal fallout related to a  
151 pulsating hydromagmatic explosive activity from a source located inside the La Fossa caldera on  
152 Vulcano island (De Astis et al, 1997; Lucchi et al., 2008, 2013b; Cicchino et al., 2011) (Fig. 1A).  
153 Also, the composition of BT, ranging from K-series ( $K_2O = 3.3-7.5$  wt.%) basaltic trachy-andesites  
154 and trachy-andesites through to tephri-phonolites and trachytes ( $SiO_2 = 49.9-64.1$  wt.%;  $Na_2O + K_2O$   
155  $= 6.5-12.6$  wt.%), is entirely consistent with the Vulcano magmatic system (Meschiari et al., 2020).



156 The BT succession is delimited at the base by marine terraces attributed to the late marine  
157 (oxygen) isotope stage (MIS) 5 (c. 124-80 ka) and is subdivided into four macro-units: Lower BT  
158 (LBT; 80-56 ka), Intermediate BT (IBT; 56-27 ka), Intermediate-upper BT (IBT-upper; 26-24 ka)  
159 and Upper BT (UBT; 24-6 ka). This subdivision is based on the occurrence of interbedded widespread  
160 regional or local marker beds, namely the ‘Ischia Tephra’, equivalent to the Y-7 marine marker tephra  
161 (Epomeo Green Tuff, 56 ka; Keller et al., 1978; Tomlinson et al., 2014), the Monte Guardia  
162 pyroclastics from Lipari (27-26 ka) and the Spiaggia Lunga scoriae (24 ka) on Vulcano (Fig. 2)  
163 (Meschiari et al., 2020). These macro-units are furtherly split into (at least) 16 depositional units, best  
164 documented on Vulcano and Lipari islands, where they have variable thicknesses ranging from a few  
165 decimetres up to a maximum of 3 m (for each depositional unit), while the entire BT succession has  
166 a (cumulated) maximum thickness of 15–25 m on Vulcano and southern Lipari. The different BT  
167 depositional units are best distinguished when they are separated by interlayered (local) volcanic units  
168 and tephra layers. Between these, the Petrazza Tuffs from Stromboli (77-75 ka) contribute to define  
169 the lower chronological constraint of the LBT, whilst the Grey Porri Tuffs (GPT, 70-67 ka) and Lower  
170 Pollara Tuffs (LPT, 27 ka) from Salina and the Vallone del Gabellotto tephra from Lipari (8.7–8.4  
171 ka) are important for stratigraphic subdivisions in the LBT, IBT and UBT, respectively (Fig. 2). The  
172 Cugni di Molinello scoria bed is an important stratigraphic marker on Vulcano separating the lower  
173 and upper portions of the UBT (De Astis et al., 1997; Lucchi et al., 2008, 2013b), which are delimited  
174 at the top by the Punte Nere tuffs (5.5 ka). A list of the main features of the units interlayered within  
175 the BT succession is provided in the Supplementary File 1. When not intercalated with other deposits,  
176 the BT generally appear as lithological homogeneous tephra accumulations that are unlikely to  
177 represent single depositional units, but instead they are the amalgamation of different depositional  
178 units, as also testified by the occurrence of interlayered localized erosional surfaces and reworked  
179 horizons with a limited lateral persistence.

180

### 181 3. METHODS AND TERMINOLOGY

182

183         Lithostratigraphic and sedimentological analysis of the BT was carried out on most of the  
184 outcrops exposed on the islands of Vulcano and Lipari (Fig. 1A; Table 1), which allow identification  
185 (and correlation) of the largest number of depositional units of the BT, relative to all the distinguished  
186 BT macro-units (LBT, IBT, IBT-upper and UBT). Following Lucchi (2013), a “depositional unit” is  
187 defined as the volcanic (pyroclastic) material deposited during a single, relatively continuous  
188 depositional event from PDCs or fallout, and is delimited by evidence of interruptions of deposition  
189 (e.g. erosive surfaces, paleo soils, reworked beds, angular discordances) or other sedimentological  
190 features (e.g. presence of fine “co-ignimbrite” ash, lithic-rich beds, sharp grain-size variations),  
191 and/or by interlayered exotic pyroclastic (including distal tephra layers) or lava deposits.

192         Outcrop description and sediment logging were based on classical lithostratigraphy and  
193 lithofacies analysis, as the main tools to infer the volcanological interpretation of the studied deposits  
194 in terms of their transport and emplacement mechanisms (see Branney and Kokelaar, 2002; Sulpizio  
195 and Dellino, 2008; Lucchi, 2013 for reviews). Sedimentological investigation of BT units was carried  
196 out through lithofacies analysis, which has commonly been used to describe and decipher the deposits  
197 of marine and non-marine environments (e.g. Miall, 1978; Lowe, 1982; Mathisen and Vondra, 1983;  
198 Miall, 1985; Smith, 1986, 1987; Waresback and Turbeville, 1990; Zanchetta et al., 2004a) and then  
199 applied to complex sequences of pyroclastic deposits (Sohn and Chough, 1989; Chough and Sohn,  
200 1990; Colella and Hiscott, 1997; Gurioli et al., 2002; Sulpizio et al., 2007, 2010) and to lateral and  
201 vertical variations of sedimentary structures within widespread ignimbrites (e.g. Freundt and  
202 Schmincke, 1986; Druitt, 1992; Cole et al., 1993; Allen and Cas, 1998). Lithofacies have been  
203 identified in the BT deposits using a combination of texture, sedimentary structures, grain-size and  
204 sorting (Table 2). Sedimentary structures were described and measured at cm-scale, and grain-size  
205 and component analyses were carried out on selected samples of the mixing bands and reworked bed  
206 material at the base of various BT depositional units. Weight % of the size fractions coarser than  $3\phi$   
207 ( $125\ \mu\text{m}$ ) at  $0.5\phi$  intervals ( $\phi = -\log_2 d$ ), where  $d$  is the particle size in mm) were estimated using dry

208 mechanical sieving. The finer fractions, from 3.5  $\phi$  (63  $\mu\text{m}$ ) to 9  $\phi$  (2  $\mu\text{m}$ ), were analysed by means  
209 of a Beckman Coulter Multisizer 4 (Mele et al., 2015), and expressed as volume % and successively  
210 converted in weight % using a constant clast density assumed equal to that of powdered BT.  
211 Component analysis (juvenile, lithics and crystals) was carried out on a representative number of  
212 particles of each grain-size fraction of the bulk material. We have differentiated six main classes of  
213 components in the size fractions coarser than 3  $\phi$  (125  $\mu\text{m}$ ): i) pumice (white and grey) and ii) scoria  
214 of different porphyricity and vesicularity; iii) obsidian fragments; iv) glass fragments; v) crystals; vi)  
215 lithic clasts. The finer size fractions are undifferentiated. For the size fractions in the range from 16  
216 to 1.4 mm, a subsample of particles of each component was hand-picked and weighted; the weight  
217 fraction of each component was calculated for each size by scaling the number of particles of the  
218 subsample to the total weight of the sample. For the grain-size range from 1 to 0.125 mm, particles  
219 of each component were counted under a stereomicroscope. The weight of each component was  
220 estimated by means of the density of each component in each size fraction. The grain-size statistical  
221 parameters by Folk and Ward (1957) were then calculated for the different sub-populations  
222 recognised in the samples from the base of BT depositional units by means of the GRADISTAT  
223 program (Blott and Pye, 2001; Table 3).

224 Major and minor element glass data for selected samples of the basal portions of a number of  
225 BT depositional units are here provided, referring to the extensive dataset recently made available by  
226 Meschiari et al. (2020) for most of the BT depositional units and the interbedded tephra deposits. The  
227 samples were mounted in Streurs Epofix epoxy resin and mounts were ground, polished and carbon  
228 coated in preparation for chemical analysis. Glass data were determined using a wavelength-  
229 dispersive JEOL 8600 electron microprobe (WDS-EMP) hosted at the RLAHA, University of  
230 Oxford. Details of the analytical operating conditions, monitoring of data accuracy and precision, and  
231 post-analysis data treatment are provided in Meschiari et al. (2020), together with the MPI-DING  
232 reference glasses (Jochum et al., 2006). Data presented in plots are normalised (e.g., water-free) and

233 error bars represent reproducibility, calculated as 2X standard deviation of replicate analysis of  
234 StHs6/80-G reference glass.

235

## 236 **4. RESULTS AND ANALYSES**

237

### 238 **4.1. Sedimentological features of the BT**

239 Sedimentological analysis of the BT has been carried out on the outcrops exposed on Vulcano  
240 and Lipari islands (Fig. 1A), which allow definition of the most complete succession of distinct  
241 depositional units of the LBT, IBT, IBT-upper and UBT macro-units (Fig. 2). Most of the outcrops  
242 are located in the flattish area of Il Piano on Vulcano island, located southeast of the La Fossa  
243 Caldera source area, and mainly belong to the UBT macro-unit. These outcrops are the most  
244 proximal today exposed, because the very proximal BT deposits within the inner part of the La  
245 Fossa Caldera were affected by the recent collapses in this area or buried below the Holocene  
246 deposits of the La Fossa cone (De Astis et al., 2013). Other outcrops of the BT are located to the  
247 west of the La Fossa Caldera, near the locality of Grotta dei Pisani, and along the southern flank of  
248 Vulcano, near Gelso (Fig. 1A). The BT have been also investigated on a number of outcrops in  
249 distinct sectors of the nearby island of Lipari at increasing distances from the source area. The main  
250 characteristics of the studied outcrops, and their distance from the source area, are summarized in  
251 Table 1.

252 In most outcrops the BT consist of massive (fine to coarse) ash and show, in places, internal  
253 bands of different colours (and grain-size) with gradual contacts (lithofacies mA; Table 2; Fig. 3A).  
254 Plane-parallel to cross bedding stratification and lamination (lithofacies psA-xsA; Table 2; Fig. 3B)  
255 occur in some exposures on Vulcano and southern Lipari islands, particularly in the UBT deposits  
256 (De Astis et al, 1997; Lucchi et al., 2008). Dune bedding with internal cross stratification (having ca.  
257 2-m wavelength and 0.5-m amplitude) are observed in the outcrops of the UBT outside the south-  
258 eastern rim of La Fossa Caldera. In the outcrops on Vulcano island, the BT are generally characterised

259 by the alternation of mm to cm thick massive and stratified beds (lithofacies altpsmA), with the  
260 occurrence of some laminae of weakly consolidated reddish fine ash. The stratification (and  
261 lamination) is generally not laterally persistent and is largely disrupted (lithofacies isA; Table 2; Figs.  
262 3C-F). A typical upward bending of the laminae is observed in many of the fragmentation points (Fig.  
263 3E-H), and in some cases disruption of the laminae occurs in correspondence of mm-scale vertical  
264 columns of coarse ash (Fig. 3G-H). The disruption of stratification (lamination) is frequently  
265 pervasive, with fragments of laminae distributed unevenly within the massive deposits. It is  
266 noteworthy that in a number of outcrops on Vulcano, although seemingly not stratified and  
267 unstructured, the BT deposits embed scattered fragments of laminae as relicts of the original  
268 stratified/laminated lithofacies (Fig. 3I).

269 Sin-depositional shear structures (lithofacies mixAL, ucAL, rfAL, ruAL; Table 2) are described  
270 and measured at cm-scale at the base of most of the BT depositional units (Figs. 4 and 5), and they  
271 are mainly recognised on Lipari rather than on Vulcano (the BT source area). This is probably because  
272 of the most common occurrence of interlayered (incoherent) exotic pyroclastic deposits within the  
273 BT succession on Lipari, which make the shear structures in the basal portions of the different BT  
274 depositional units more evident. In these cases, the basal contacts between BT and exotic deposits are  
275 transitional (Fig. 4) and occur as bands of mixed material between the BT and the underlying  
276 incoherent pyroclastic deposit (lithofacies mixAL; Table 2). Most of the interbedded pyroclastic  
277 deposits are composed of whitish to grey pumice and obsidian of local origin (Punta di Perciato,  
278 Falcone, Lip1, Monte Guardia, Vallone del Gabelotto) or grey to dark-grey scoriae and pumice from  
279 Salina (Grey Porri Tuffs and Lower Pollara Tuffs), which show a strong lithological contrast with  
280 respect to the homogeneous reddish-brown to grey, ash characterizing the BT (Fig. 4). Where two  
281 BT depositional units directly overlie each other without a distinguishing layer of exotic pyroclasts,  
282 the original thickness and limit between the units cannot be easily recognised (e.g., Fig. 3A), unless  
283 it is marked by a minor erosive surface, as occurs in places (Lucchi et al., 2008). This seems the case  
284 of the island of Vulcano where the succession of BT is generally made up of distinct, amalgamated

285 depositional units, interlayered only occasionally with exotic pyroclastic deposits. On Vulcano,  
286 visible mixing bands occur only when BT units overlie the whitish pumice lapilli and ash of the Monte  
287 Guardia and Vallone del Gabellotto fall deposits (Fig. 4G, H) or dark-grey scoriae of the Cugni di  
288 Molinello unit. Note that the base of the BT depositional units is sharp when they overlie lavas or  
289 welded scoriae and other non-erodible pyroclastic deposits, whilst the top contact of BT where they  
290 are overlain by other exotic deposits is always sharp (conformable or unconformable).

291 Over the entire study area (from northern Lipari to southern Vulcano) the lithofacies mixAL  
292 occurs independently of the paleo-topography, outcropping even in case of a sub-horizontal paleo  
293 topography. Thickness of the mixing bands ranges (approximately) from a few to tens of cm, with a  
294 gradual upward transition to the un-mixed BT material (Fig. 4; Table 1) and is arbitrarily measured  
295 relative to the level where the original component of BT is dominant with respect to the incorporated  
296 clasts from the underlying units. The mixing bands are generally massive, but they show in places  
297 alignments of lapilli. The maximum dimension of entrained clasts (either pumice, scoria or lithic) is  
298 generally of fine to medium lapilli, although they can occasionally reach sizes of 10 cm (e.g., at the  
299 base of BT9 depositional unit in southern Lipari; Fig. 4E). The entrained clasts may be uniformly  
300 distributed within a whole BT depositional unit, even if scattered (e.g., Fig. 4F), but in most cases  
301 their abundance decreases regularly upwards. When the range of grain sizes of the entrained clasts is  
302 broad, reverse grading of the coarse clasts is observed (e.g., Fig. 4E).

303 Undulated structures consist in basal layers composed of mixed material between the BT and  
304 the underlying incoherent pyroclastic deposit that appear as wavy and consisting of alternating crests  
305 and troughs (lithofacies ucAL; Table 1). They are recognised in southern and central Lipari at the  
306 contact between BT and the underlying pumice units (Fig. 5A-C). Following Pollock et al. (2019),  
307 the length of an undulated structure is the distance between successive troughs, and its height is the  
308 distance from the lowest part of a trough to the top of the crest. Undulated structures on Lipari have  
309 length between 60 and 450 cm and height of ca. 20 cm (Table 1), and they are best exposed in outcrops  
310 arranged longitudinally with respect to the BT source area, at distances of 7-10 km (Fig. 5A-C). Crests

311 are almost symmetric and internally massive (Fig. 6B), showing imbrication of coarser clasts in the  
312 upper part of the mixed material.

313 Recumbent flame structures (lithofacies rfAL; Table 2) have an overhanging arm of entrapped  
314 clasts from the basal layer that protrudes up into the BT deposit and becomes sub-horizontal and thins  
315 in downflow direction (conforming with Pollock et al., 2019). They look very similar to the ‘shark  
316 fin’ structures of Douillet et al. (2019). Recumbent flame structures are common at the base of  
317 depositional unit BT9, with the best preserved one documented above the Falcone pyroclastic  
318 deposits at Spiaggia Valle Muria, south of Lipari, where the structure has a length of about 60 cm and  
319 height of about 20 cm (Fig. 5D). The length is the extent of the deformed zone and the height is the  
320 distance from root to top of the sub-horizontal tail. Lithofacies rfAL commonly occurs as trains of  
321 pumice and lithic lapilli a few cm above and parallel to the basal contact of the depositional unit BT9  
322 (Fig. 5D). In places, only the trunk of the structure is preserved as an asymmetric deformation of the  
323 lapilli from the underlying bed (Fig. 5E).

324 Rip-up structures (lithofacies ruAL; Table 2), similar to recumbent flame structures, are visible  
325 at the base of some depositional units. In these cases, the contact is almost planar, but there are small  
326 hook-like structures as asymmetric deformations of the underlying bed, which resemble the trunk of  
327 a flame structure (Fig. 5F). These structures are usually few cm in height, and they are bended  
328 downcurrent.

329

330

#### 331 **4.2. Grain-size and components of the mixing bands of the BT**

332 We collected samples of the mixing bands at the base of some BT depositional units on Lipari  
333 island, with the aim of investigating their grain-size distribution and components. The depositional  
334 units investigated here cover mostly the stratigraphic interval of the IBT and IBT-upper macro-  
335 units, but, as for the grain-size distributions, the results may be considered representative of the

336 entire BT succession because of similar lithology and textural characteristics (Lucchi et al., 2008;  
337 De Rosa et al., 2016).

338 Most samples have a polymodal grain-size distribution (except for sample Lip03/17) and a  
339 large number of components (Fig. 6), as widely expected for mixing bands between BT units and  
340 the underlying tephra beds. In this respect, each grain-size distribution is the combination of two  
341 distinct sub-populations of components, one referred to the BT and the other relative to the  
342 underlying pyroclastic deposits. Considering that the Folk and Ward (1957) statistical parameters,  
343 like median diameter ( $Md\phi$ ) and sorting ( $\sigma\phi$ ), are not useful for polymodal distributions, we then  
344 calculate them in Table 3 for the separated component distributions (and not for the bulk grain-size)  
345 recognised in the samples from the base of BT depositional units as in Figure 6.

346 The BT typically consist of fine (dominant) to coarse ash composed of aphyric, glass  
347 fragments (from about 65 to 90 vol. %), from dark brown to brownish and colourless, mostly  
348 blocky or poorly vesicular, often slightly altered on their external parts (De Astis et al., 1997; De  
349 Rosa et al., 2016). The rest of the BT juvenile components (5–35%) are crystals (clinopyroxene and  
350 minor plagioclase, K-feldspar, olivine and amphibole) that are presents as loose fragments or  
351 rimmed by glass, with local abundance of mm-size clinopyroxene crystals. Lithic fragments are  
352 subordinate in the BT as components of the coarse ash fraction, for a total lithic content usually  
353 lower than 5 vol.% (De Astis et al., 1997; Lucchi et al., 2008; De Rosa et al., 2016), except for  
354 higher amounts up to 10% in some outcrops of the UBT on Vulcano (De Astis et al., 1997).  
355 Diffused dark (to yellowish) scoria lapilli are recognised in different stratigraphic levels of the BT  
356 on Vulcano and Lipari (Meschiari et al., 2020).

357 In carrying out the componentry analyses, we attributed most of the glass fragments and  
358 crystals recognised in the fine to coarse ash fractions to the juvenile BT sub-population, along with  
359 the (undifferentiated) very fine ash. Loose crystals are considered as components of the BT sub-  
360 population, because they lack in the units interlayered to the BT succession. Lithics are kept aside  
361 from this analysis because it is not possible to establish which sub-population they belong to. The



362 analysed samples contain variable amounts of exotic components that are correlated to the  
363 pyroclastic deposits underlying each of the BT depositional units. These are classified here as  
364 'external components' with respect to the BT sub-population. Specifically, whitish to (minor) grey  
365 pumice, and obsidian fragments are recognised in the mixing band at the base of depositional unit  
366 BT9 (outcrop L2) and they are fully consistent with the componentry of the underlying Falcone  
367 tephra (Gioncada et al., 2005; Forni et al., 2013). Poorly vesicular, highly porphyritic dark scoria  
368 and highly vesicular (sub-aphyric) white pumice are reported in the mixing band at the base of  
369 deposition unit BT11 in the outcrop L12, as the main components of the underlying bed of the  
370 Lower Pollara Tuffs from Salina Island (Morche, 1988; Crisci et al., 1991; Calanchi et al., 1993;  
371 Lucchi et al., 2008; Forni et al., 2013). Then, the base of depositional unit BT12 sampled in the  
372 outcrops L5, L10 and L12 contain highly vesicular, white (Kf-bearing) pumice, dense to moderately  
373 vesicular grey pumice and banded pumice, and variable amounts of obsidian fragments and lithic  
374 clasts that are the typical components of the underlying Monte Guardia pyroclastic deposits (De  
375 Rosa et al., 2003). A certain amount of sub-aphyric, dark scoria ash fragments are recognised in the  
376 depositional units BT9 and BT12 (in outcrops L2, L5 and L10), and they are not present in the  
377 underlying Falcone and Monte Guardia units. These scoria fragments are thus included in the  
378 componentry of the BT depositional units, in agreement with the report of diffused dark scoria  
379 lapilli in different BT outcrops on Vulcano and Lipari (Meschiari et al., 2020). In all the analysed  
380 BT depositional units the exotic components are prevalent in the lapilli and block/bombs fractions  
381 (Fig. 6), and they have a polymodal grain-size distribution. Glass fragments, crystals and scoria  
382 referred to the BT are instead mainly represented in the fine ash fraction. There is not a significant  
383 variation of the relative abundance of exotic components with distance from the source area, as  
384 evident comparing the grain-size distributions of the BT12 depositional unit in the outcrops L5, L10  
385 and L12 (Fig. 6), at distances from 10 to 14.5 km from the source. However, different quantities of  
386 the single grain-size classes and variations of the content of the individual exotic components are  
387 reported in these outcrops as a function of the variable lithological features of the underlying Monte

388 Guardia unit in proximal to distal reaches, relatively to the eruptive vent in southern Lipari.  
389 Significant vertical variations of the grain-size parameters are reported for data from different levels  
390 of the same BT depositional unit. Specifically, BT12 in the L5 outcrop and BT11 in outcrop L12  
391 were sampled at two stratigraphic levels (Fig. 6), and component analyses show an upward decrease  
392 of the content of exotic components, along with an increase in the amount of fine ash.

393 The analysed sub-populations of the BT, largely devoid of exotic clasts, have all fairly regular  
394 and unimodal grain-size distributions, with generally good to moderate sorting ( $\sigma_\phi$  ranging between  
395 1.29 and 2.07) and  $Md_\phi$  ranging between 3.13 and 4.97 (Fig. 6). These values are roughly consistent  
396 with the pattern obtained by De Astis et al. (1997) for the UBT on Vulcano which defines a trend of  
397 regularly decreasing median and better sorting from proximal ( $\sigma_\phi=0.8-1.8$  and  $Md_\phi=1.7-2.5$  at  
398 distances of 1.5-2.0 km) to more distal locations ( $\sigma_\phi=1.0-1.2$  and  $Md_\phi=3.0-3.5$  at distances of 4.0-  
399 4.5 km) from the source. However, not all BT samples on Lipari fit this trend perfectly, as shown  
400 for example by the median value of 1.98 for the LIP02/17 sample in central Lipari and the moderate  
401 sorting of some samples in different sectors of Lipari. On this, we argue that the data for the BT  
402 sub-populations may be not totally depurated from the presence of external components related to  
403 the embedded lapilli and ash from the underlying units.

404 We also calculated the Sauter mean diameter (Sauter 1926) of the different grain size  
405 distributions (Table 3). The Sauter mean diameter is a length-scale parameter useful in  
406 characterizing fluidization processes in granular materials (Kowalczyk et al., 2016), because it  
407 defines the area-weighted mean particle size, which is important to estimate the drag applied onto  
408 particle surfaces. Because our BT sub-populations are mostly unimodal and Gaussian like, we used  
409 the method of Breard et al. (2019):

410

$$411 \quad D_{32}(mm) = 2^{-[\mu_\phi + \frac{\ln 2}{2} \sigma_\phi^2]} \quad (1)$$

412

413 where  $\mu_{\phi}$  is the mean of the grain size distribution and  $\sigma_{\phi}$  is the sorting. The values of the Sauter  
414 mean diameter of BT sub-populations range from 0.22 mm to 0.03 mm (Table 3), which results in a  
415 minimum permeability in the order of  $10^{-10} - 10^{-12} \text{ m}^2$  (Breard et al., 2019).

416

### 417 **4.3. Geochemical components of the mixing bands of the BT**

418 A number of the BT depositional units investigated on both Lipari and Vulcano islands  
419 contain minor populations of exotic volcanic glass compositions that mostly plot well outside the  
420 dominant K-series compositional field of the BT, which ranges from basaltic trachy-andesites and  
421 trachy-andesites through to tephri-phonolites and trachytes. The exotic glass compositions are here  
422 named ‘secondary components’ consistent with Meschiari et al. (2020) (Fig. 7A, B). These  
423 secondary components are generally reported from the basal portions of the individual BT  
424 depositional units, characterised by mixing bands with the underlying pyroclastic deposits  
425 (lithofacies mA), and chemically similar to these deposits. Figure 7 provides clear evidence of the  
426 geochemical correspondence between the secondary components identified within depositional  
427 units belonging to the LBT, IBT, IBT-upper and UBT macro-units and the underlying pyroclastic  
428 units sourced from eruptions on Salina (Grey Porri Tuffs), Lipari (Punta del Perciato, Falcone, Lip1,  
429 Monte Guardia, Vallone del Gabellotto) and Vulcano (Cugni di Molinello), following the  
430 reconstructed stratigraphic succession (Fig. 2). Major and minor element glass analyses of  
431 representative samples relative to different BT depositional units and their secondary components  
432 are reported in the Supplementary File 2.

433 Among the analysed samples there is only one apparent lack of geochemical agreement  
434 between a BT secondary component and the underlying deposits. Specifically, the BT8 depositional  
435 unit (sample bt12/16), belonging to the IBT, directly rests above the Punta del Perciato pumice and  
436 ash in the L2 outcrop of Lipari. While it contains secondary rhyolitic glasses that are  
437 compositionally similar at a major element level to the Punta del Perciato glasses, some of these  
438 secondary glasses exhibit significantly higher  $\text{K}_2\text{O}$  and lower  $\text{Na}_2\text{O}$  contents relative to the Punta

439 del Perciato glasses (Figs. 7C, D, E). These offsets could reflect compositional variability in the  
440 underlying Punta del Perciato tephra unit which may have been previously undetected, considering  
441 that its previous chemical characterisation targeted only the pumice component (Albert et al., 2017).  
442 An alternative explanation is that hydration has resulted in alkali exchange within these particular  
443 glass fragments. This is apparently supported by previous IBT investigations by De Rosa et al.  
444 (2016) who identified physical evidence of fluid induced alteration (hydration) of the juvenile glass  
445 particles relating to the sin-eruptive interaction of magma and hot fluids or seawater. Indeed, our  
446 attempt to chemically analyse juvenile glass components of BT8 was entirely precluded by the  
447 significant alteration of the dominant glass component.

448         It is noteworthy that in some cases secondary components are also reported in BT  
449 depositional units where mixing with underlying pyroclastic deposits is not visible at a macroscopic  
450 scale. In south Lipari (outcrop L2) we sampled the IBT (sample bt14/16) that rests above the  
451 Falcone pumice succession, which are commonly subdivided into the depositional units BT9 and  
452 BT10 by the interlayered Lip1 tephra unit (Fig. 2). The sample bt14/16 contains HKCA rhyolitic  
453 secondary glass components that are broadly consistent with the Lip 1 ash (Figs. 7C, D, E),  
454 although this tephra layer is not visible in the investigated outcrop. A possible correlation of the  
455 HKCA rhyolitic secondary glass components found in bt14/16 with the underlying Falcone pumice  
456 unit is considered not probable because this sample was taken close to the base of the (overlying)  
457 Lower Pollara Tuffs, at about 2 meters above the contact with the Falcone unit. A similar situation  
458 is noticed at the Punta della Crapazza outcrop (L0) in the IBT sampled above the Falcone domes  
459 (samples LIP15/18, LIP16/18). In these samples we do observe HKCA rhyolitic secondary glasses  
460 which are chemically consistent with the Lip1 tephra layer (Figs. 7C, D, E), although the latter is  
461 not visible in the investigated stratigraphic succession. A correlation of these secondary components  
462 with the Falcone unit, which could be chemically possible, is considered unreasonable because the  
463 sampled IBT rests above the thick lava domes erupted after the Falcone pumice succession. Finally,  
464 at the outcrop of Monterosa (L7) we sampled the IBT (sample LIP45/17) above the Ischia Tephra,

465 and none of the interbedded stratigraphic markers from southern Lipari are visible (e.g., the Punta di  
466 Perciato, Falcone and Lip1). However, in sample LIP45/17 we do find chemical evidence of  
467 secondary HKCA rhyolitic glass components that could be attributed to any of the above-mentioned  
468 tephra units (Figs. 7C, D, E).

469

## 470 **5. DISCUSSION**

471

472 In the following, we will discuss the evidence of an origin of the BT deposits on the islands of  
473 Vulcano and Lipari from PDCs, and their specific transport and depositional mechanisms. We will  
474 not include in this discussion the BT deposits cropping out on other islands of the Aeolian  
475 archipelago or in the Sicily mainland, which do not have the same characteristics of lithofacies  
476 indicative of a PDC deposition. On this, we rely on the previous interpretation that the BT  
477 recognized further distally from the La Fossa Caldera source in the other islands of the Aeolian  
478 archipelago and Capo Milazzo in Sicily reflect fallout processes from a pulsating eruption column  
479 or co-ignimbrite ash clouds (Lucchi et al., 2008), whilst distal ash layers are recorded in Tyrrhenian  
480 and Adriatic Sea marine cores (Meschiari et al., 2020). This reflects the high mobility of fine ash in  
481 the atmosphere, which can be dispersed by both high and low atmosphere dynamics due to their  
482 long settling times (Sulpizio et al., 2008b; 2013; Giaccio et al., 2008).

483

### 484 *5.1. Model for deposition from the BT PDCs*

485 PDC deposits record processes occurring in the flow boundary zone, which includes the  
486 lowermost part of the current interacting with the forming deposits or with the topography (Branney  
487 and Kokelaar, 2002). Most PDC deposits originated from stratified flows in which the segregation  
488 of the particles with higher terminal velocities in the lowermost part can result in the development  
489 of a high concentration zone (Valentine, 1987; Branney and Kokelaar, 2002; Dellino et al., 2004;  
490 Sulpizio et al., 2014). This basal portion of the flow can move downslope developing different

491 depositional regimes, which can span from traction- to granular flow-dominated (see Branney and  
492 Kokelaar, 2002; Sulpizio et al., 2014; Lube et al., 2021; for a review of internal structures and  
493 processes). In polydisperse mixtures, including a wide range of sizes (from ash to blocks) and  
494 componentry (lithics, pumice, crystals), sedimentary structures may help in deciphering the  
495 depositional regime at time of deposition, defining the lithofacies of the deposit. As an example,  
496 sedimentary structures like parallel to cross stratification and dune-bedding are indicative of  
497 traction-dominated depositional regime from a flow-boundary zone of a diluted PDC (e.g., Andrews  
498 and Manga, 2012; Doulliet et al., 2019). At the other end of PDC spectrum, reverse grading of  
499 coarse clasts may indicate a granular flow-dominated depositional regime in a concentrated PDC, in  
500 which grain interaction can induce kinetic sieving and kinematic squeezing of the largest particles  
501 (e.g., Felix and Thomas, 2004). If the porosity within the flow-boundary zone is sufficiently low to  
502 maintain the gas entrapped in the mixture, a fluid escape-dominated depositional regime may  
503 develop, with deposits that appears massive and poorly sorted. Well selected, ash dominated  
504 deposits are generally interpreted as gentle settling of fine-grained particles from a diluted cloud,  
505 defining a direct fallout regime.

506         These sedimentological hints are of little significance to interpret the features of PDCs formed  
507 only by well selected ash particles, as in the case of most of the BT deposits (Figs. 3-5). This is  
508 because of the impossibility to develop sedimentary structures from very fine grain-sizes (Dellino et  
509 al., 2019), which makes difficult to interpret the depositional regimes of ash-rich PDCs from  
510 lithofacies analysis. This is one of the reasons why it is complicated to decipher the transport and  
511 depositional mechanisms of the PDCs of the BT eruptions, which were previously generically  
512 interpreted as mostly dilute PDCs or fallout from co-ignimbrite ash clouds or accompanying  
513 eruption columns (De Astis et al., 1997; Lucchi et al., 2008).

514         Most of the information on the depositional mechanisms of the BT presented here is derived  
515 from distinctive lithofacies mA, psA and xsA (Table 2) recognised in the proximal outcrops of the  
516 UBT macro-unit on Vulcano island (outcrops V1-V4; Fig. 1A). Massive deposits of the lithofacies

517 mA are interpreted as the result of the deposition from slow-moving, ground-hugging ash-rich  
518 PDCs, and their homogeneous appearance is indicative of fluid escape or granular flow depositional  
519 regimes from a fine-grained, concentrated flow-boundary zone. The abundant ash aggregates  
520 present in these deposits at the microscopic scale (Lucchi et al., 2008) indicate the occurrence of  
521 steam in the ash cloud or fine ash aggregation driven by electrostatic force during the gentle settling  
522 of ash from the more diluted portions (or the phoenix cloud) of the PDCs. Lithofacies psA and xsA  
523 instead indicate grain by grain deposition from dilute and turbulent PDCs, mainly formed by coarse  
524 and fine ash, in which suspension and traction are the main transport (and depositional)  
525 mechanisms. Notably, in the UBT deposits investigated here, the most common is lithofacies  
526 altpsmA (Fig. 3; Table 2). This is a combination of lithofacies mA and lithofacies psA, and is  
527 indicative of a stepwise, repetitive aggradation of discrete PDC pulses developed within each  
528 depositional unit of the BT. Massive beds are deposited from granular- or fluid-escape dominated  
529 depositional regimes of concentrated PDCs and alternate with stratified ash from the turbulent and  
530 diluted ash cloud accompanying the underflow during the waning stage of each pulse. This  
531 depositional behaviour is consistent with the long-lasting, pulsating eruptive activity that is assumed  
532 to have characterised the emplacement of the UBT macro-unit (and the rest of the BT) on Vulcano  
533 island (Lucchi et al., 2008, 2013b).

534       However, intermittently stratified ash deposits of the lithofacies isA (Fig. 3) are the most  
535 prominent on Vulcano island and characterise most of the BT outcrops on Il Piano area. This  
536 lithofacies is not interpreted as a primary feature acquired at time of deposition of the PDCs during  
537 the BT eruptions, but as the result of pervasive post-depositional disruption of the primary deposits  
538 of lithofacies altpsmA. The disruption of stratified beds here is explained as due to fluid escape  
539 related to dissipation of pore pressure from the underlying massive beds occurred during or  
540 immediately after the emplacement of the individual beds (Fig. 8). This mechanism of fluid  
541 expulsion resembles that largely described in marine and fluvial sedimentary environments (Allen,  
542 1977; Owen, 1987; Selker, 1993; Owen, 1996; Odone et al., 2011), and even in pyroclastic

543 deposits (Douillet et al., 2015). Experiments have demonstrated that fluid expulsion structures can  
544 be produced by an unstable fluidization behaviour where a lower base layer of granular material is  
545 inhibited from releasing intergranular fluids by the presence of an overlying low porosity top layer  
546 (Nichols et al., 1994). The weight of the overlying material is balanced by an increased fluid  
547 pressure in the basal layer. If the load exceeds a critical threshold, a fluid-filled crack forms and, as  
548 it grows, instability causes the top layer to bend (Fig. 3G). Rupture occurs at the apex of fluid crack,  
549 allowing the underlying fluid and fluidized material to burst out through the top layer. The fluidized  
550 base layer material then flows through the rupture until the fluid overpressure is fully dissipated.  
551 The top layer material is bent upwards around the rupture (Figs. 3E, G, H), and the resulting pillar-  
552 type escape structure is preserved (Figs. 3G, H). The vigour of the burst out is greatest when the  
553 base layer material has a grain-size 15% of the top layer material (Nichols et al., 1994), as in the  
554 case of the BT investigated here that are composed of coarse to fine ash deposits. If the base layer  
555 grain-size is less than 8% of the top layer then base layer material will pass through the top layer  
556 pore spaces, without forming an escape structure. Depending on how much the disruption  
557 mechanism was pervasive, the BT deposits in the investigated outcrops have either largely  
558 preserved the original lithofacies (Fig. 3F) or they are almost entirely massive with only fragments  
559 of laminae distributed unevenly as relicts of the original stratified lithofacies (Fig. 3I). It is therefore  
560 important to note that in many cases the massive deposits of the BT on Vulcano are not a primary  
561 lithofacies, but they are instead the result of pervasive post-depositional fluid escape processes  
562 occurred during or immediately after their emplacement. De Astis et al. (1997) suggested that the  
563 fragments of stratified ash embedded in some massive BT deposits was due to fragmentation of a  
564 stratified layer due to an external trigger (earthquakes), with subsequent sinking of the denser and  
565 heavier fragments into the soft massive deposits. We consider this explanation less probable  
566 because the evidence of disrupted stratification and fragments of stratified ash is recognised in a  
567 number of BT depositional units at different stratigraphic levels, which makes it difficult to assume  
568 a repetitive trigger external to the depositional system. Moreover, the upward bending of the



569 fragmentation points and pillar-type structures observed in the lithofacies isA are more consistent  
570 with a model of fluid escape. Small ash diapirs were explained by De Astis et al. (1997) as a result  
571 of a significant amount of (liquid) water in the massive deposits, but we consider more probable a  
572 process of fluid escape due to dissipation of the pore pressure during deposition of the BT and  
573 subsequent compaction.

574 Most of the BT outcrops on Lipari and southern Vulcano are characterised by homogeneously  
575 massive lithofacies that are referred to deposition from PDCs on the base of significant thickness  
576 variations as function of paleo-topography of the individual BT depositional units, which is not fully  
577 consistent with primary fallout processes (Lucchi et al., 2008). Progressive aggradation of different  
578 PDC pulses can be argued from faint banding due to colour differences or subtle grain-size variations  
579 within massive deposits. Also, in this case the deposits are mostly formed by ash, which raises the  
580 issue if they were erupted as mixtures of fine particles or if the coarse particles were deposited in very  
581 proximal areas. It was suggested that an efficient hydromagmatic fragmentation have produced a  
582 large amount of fine ash with respect to lapilli and blocks. Evidence that fragmentation was driven  
583 mostly by magma-water interaction is provided by SEM results showing that equant blocky  
584 fragments, with quenching cracks and abundant adhering particles are dominant in the BT deposits  
585 (De Astis et al., 1997; Lucchi et al., 2008). This is consistent with a location of eruptive vents inside  
586 the La Fossa Caldera, the floor of which might have been below or near sea level during most of its  
587 evolution starting from c. 80 ka (De Astis et al., 2013). Another possible explanation, which may be  
588 concomitant with efficient hydromagmatic fragmentation, is that coarse-grained material has been  
589 probably deposited in the caldera depression, which is now filled and completely covered with the  
590 more recent deposits of La Fossa cone (De Astis et al., 1997; Lucchi et al., 2008). For the deposits  
591 outcropping on Vulcano island, it must be considered that decoupling of basal (coarse-grained) and  
592 upper (fine-grained) parts of the PDCs has occurred when the PDCs impacted against the caldera  
593 walls (Fig. 8), with only the finer grained parts transported by turbulence in the ash clouds able to  
594 overpass the topographic obstacle and spread over the central and southern parts of Vulcano island.

595           The massive BT deposits can be interpreted either as the result of direct fallout-dominated flow-  
596 boundary zones or fluid-escape (or even granular flow) depositional regimes in well sorted, ash-  
597 dominated pyroclastic mixtures (cf. Branney and Kokelaar, 2002; Sulpizio et al., 2007; 2010). Direct  
598 fallout implies mainly vertical gentle settling of particles in a slow moving or motionless pyroclastic  
599 cloud, whilst deposition from granular flow or fluid-escape dominated flow-boundary zones implies  
600 lateral movement of the moving flow. The key feature for establishing a depositional mechanism  
601 from laterally spreading PDCs is the evidence at the base of the BT depositional units of mixing bands  
602 containing a substantial component of ash and lapilli made up of pumice, scoria and lithics from the  
603 underlying pyroclastic deposits (lithofacies mixAL; Fig. 4). These mixing bands indicate erosion and  
604 incorporation of loose material from the underlying beds into the moving ash flows that deposited the  
605 BT. The general poor sorting and massive appearance of the mixed deposits are suggestive of  
606 sedimentation from a current in which the rate of supply ( $R_s$ ) is higher than the rate of deposition  
607 ( $R_d$ ), which induces rapid development of a highly concentrated zone above the flow boundary,  
608 dominated by a granular flow (or fluid-escape) depositional regime. The moving flows relative to the  
609 BT exerted shear stress over the loose, erodible pyroclastic deposits that represented their substratum,  
610 causing entrapment of exotic clasts into the flow body (Fig. 9). The reverse grading of entrained  
611 coarse clasts observed in some places (e.g. Fig. 4E) suggests that a lateral movement under high shear  
612 occurred during transportation and deposition of the BT PDCs. Such reverse grading of coarse clasts  
613 is attributed to dispersive pressure processes induced by grain-grain collision in a high-concentration  
614 zone at the base of the current (Lowe, 1982; Sohn, 1997; Dellino et al., 2004).

615           Clast embedding at the base of BT deposits was previously signalled by Lucchi et al. (2008)  
616 only in the outcrops of southern Lipari and Gelso (south Vulcano; Fig. 1A), whilst here we document  
617 the occurrence of entrainment processes across the entire study area, from northern Lipari to central  
618 and southern Vulcano, thus substantially enlarging the area where there is evidence of substrate  
619 erosion exerted by the BT PDCs. The mixing bands are easily recognised in the field where the  
620 eroded/remobilized bed is made of lapilli (due to the contrasting grain-size) or light-coloured clasts

621 (due to contrasting colour), as also supported by grain size and component analyses of selected base  
622 layers of BT depositional units (Fig. 6). When the mixing material is not visible at visual inspection,  
623 it can be documented by secondary glass components plotting outside of the main compositional field  
624 of the BT (Fig. 7). As an example, the rhyolitic Lip1 (ash) tephra layer from an eruptive vent in  
625 southern Lipari is characterised by a very discontinuous areal distribution. This can be due to  
626 processes of wind-reworking or post-depositional erosion, as typically occurs for ash beds, but the  
627 role played by processes of erosion and clast incorporation by the BT currents is clearly outlined by  
628 the finding of secondary components chemically correlated to Lip1 within the BT depositional unit  
629 above (Fig. 7C-E), even where there is no direct evidence of the Lip1 tephra layer in the field.

630 Overall, sedimentological analyses, combined with grain-size, componentry and geochemical  
631 investigation, provide unequivocal evidence that the BT were deposited from PDCs laterally  
632 spreading from the La Fossa caldera all over the islands of Lipari and Vulcano. De Rosa et al. (2016)  
633 suggested that mixing bands are the result of post-eruptive remobilization of the BT deposits on pre-  
634 existing steep slopes. The occurrence of mixing bands even on flat topography make us confident in  
635 excluding reworking as a primary mechanism. Notably, the evidence of mixing bands at the base of  
636 distinct BT depositional units even in the northern sector of the island of Lipari enlarges the area  
637 where the PDCs that deposited the BT had a potential of eroding the substratum and embedding clasts  
638 from the underlying units up to distances of 16-17 km from the source area, therefore substantially  
639 increasing the estimate of the maximum run-out of currents of this type. This is coherent with  
640 experimental models (Girolami et al. 2008; Roche et al. 2008; Cagnoli and Romano 2010; Dellino et  
641 al. 2019) showing that PDCs transporting mostly fine ash, like those of the BT on Lipari, may travel  
642 further and possess a higher capacity of impact over the territory with respect to those characterised  
643 by coarser material. On this, the calculated values of Sauter median diameters (Table 3) indicate very  
644 low porosity of the BT pyroclastic mixture in the flow boundary zone (in the order of  $10^{-10}$ – $10^{-12}$  m<sup>2</sup>),  
645 which suggests long time retention of gas within the mixture enhancing fluidization and flow mobility  
646 (Druitt et al. 2007; Smith et al., 2018; Lube et al. 2019; Roche et al., 2021).

647 It cannot be excluded that a significant part of proximal to medial massive BT deposits on  
648 Vulcano and Lipari, where evidences of shear structures or exotic component mixing are absent, is  
649 the result of ash fallout from co-ignimbrite ash clouds or eruption columns, a process that is suggested  
650 to be dominant in the more distal outcrops in the other islands of the Aeolian archipelago and the  
651 Capo Milazzo peninsula. Given the cryptic nature of the BT deposits where the contacts between  
652 different depositional units cannot be easily recognised, the volume fraction of the ash deposits  
653 possibly deposited from fallout processes could not be discerned. This does not weaken the evidence  
654 from sedimentological characteristics, which indicates a dominant deposition of the BT on Lipari and  
655 Vulcano from ground hugging PDCs.

656 The fine-grained, well sorted grain size of BT deposits is unusual for PDCs deposits recognised  
657 widely and apparently crossing between adjacent islands and deserves some further consideration and  
658 discussion. It is notable that the islands of Vulcano and Lipari are currently separated by the narrow  
659 and shallow sea-water inlet of Bocche di Vulcano with a minimum depth of c. 40 m and width of less  
660 than 1 km. Considering that most of the 80-6 ka time-stratigraphic interval of the BT has elapsed in  
661 lowstand conditions (Rohling et al., 2014), this sea-water inlet might also have been for a long time  
662 narrower and shallower. This means that most of the PDCs that deposited the BT on Lipari mainland  
663 had to overcome a small sea inlet which did not actually hinder their lateral spreading but might have  
664 influenced their transport and depositional behaviour. The PDCs that passed over the sea inlet in fact  
665 had to have density lower than sea water (i.e., less than  $1025 \text{ kg/m}^3$ ). This is an unrealistic density for  
666 the basal part of any PDCs, in which the density stratification induces packing of solid particles with  
667 density usually in excess of that of water. Therefore, it can be reasonably assumed that the basal,  
668 coarser and more concentrated portion of PDCs spreading from Vulcano sunk into the sea water  
669 accompanied by decoupling of the turbulent, more diluted portion of the PDCs which was able to  
670 pass over the sea and reach the Lipari mainland (Fig. 10). This water density bias and the decoupling  
671 of the basal and upper portions of the PDCs could explain the grain size characteristics of the BT  
672 deposits on Lipari island. When these PDCs reached Lipari they encountered a rugged and irregular

673 topography due to the presence of a rhyolitic dome complex emplaced between c. 50 and 20 ka. The  
674 flow of diluted and turbulent PDCs over variable slopes produced loss of momentum, which reflected  
675 in loss of turbulence and less capacity to maintain solid particles in suspension. This produced an  
676 increased concentration of particles in the flow boundary and transition to dominant granular flow or  
677 fluid-escape regimes at time of deposition (Fig. 10). Lithofacies analysis indicates that the BT PDCs  
678 mostly deposited in granular flow or fluid escape regimes due to interaction with the paleo-  
679 topography and increased sedimentation rate, whilst the currents travelled large distances in a dilute  
680 and turbulent behaviour reaching distances around 16-17 km from the source (up to northern Lipari).  
681 The (more) concentrated basal portions of these PDCs were generally able to erode the incoherent  
682 substratum embedding clasts from the underlying units and produced sin-depositional shear structures  
683 (see below). In any case, the distance travelled by PDCs (around 16-17 km) suggests high mass  
684 discharge rates feeding the currents spreading from the vent (Roche et al., 2021).

## 685 686 *5.2 Physical characteristics of the PDCs inferred from shear structures*

687 In addition to the mixed lithofacies, also the sedimentary structures of lithofacies ucAL, rfAL,  
688 ruAL recognised in outcrops of southern and central Lipari are indicative of an effective lateral  
689 transport and shear stress exerted by the ash flows of the BT over the substratum (Fig. 9).  
690 In particular, the undulated contacts (lithofacies ucAL) between the BT depositional units and the  
691 underlying lapilli beds in outcrops L1 and L5 may be referred to conditions of high shear stress  
692 exerted by the overriding currents to the loose lapilli substratum, which induces remobilization of  
693 its upper part and formation of waves with variable wavelength and imbrication of coarser clasts.  
694 Such imbrication testifies for the occurrence of traction carpet processes, in which the static bed  
695 material is moved and reorganised in a frictional regime by the overriding flow (e.g. Sohn, 1997;  
696 Dellino et al., 2004). Recumbent flame structures (lithofacies rfAL) also indicate high shear stress  
697 exerted by the overriding PDCs of the BT eruptions over the underlying lapilli beds, which produce  
698 incorporation of lapilli that are aligned downflow and bended to form an alignment of lapilli within

699 the BT ash deposit for a distance up to some meters. Instead, the small hook-like structures of the  
700 lithofacies ruAL is related to conditions of moderate shear stress exerted from the overriding ash  
701 flow, which was able to rip-up lapilli from the underlying bed into the BT unit but with no  
702 significant lateral displacement of the upper part of the structure. The formation of the different  
703 shear structures depends on both flow and erodible deposit characteristics, like flow velocity,  
704 depositional regime, perpendicular load component of the moving flow, grain packing in the  
705 deposit, and terminal velocity of erodible clasts, among others. Currently, there are few laboratory  
706 experiments on entrapment of loose substratum into the moving flow, carried out using synthetic  
707 material (Roche et al. 2013, 2016; Roche 2015). They mainly focus on clast entrapment due to  
708 underpressure at the head of the moving flow, a process different from that here described, which  
709 does not produce the observed syn-depositional shear structures. In order to unravel the flow  
710 conditions responsible of the various deposit characteristics and structures some hints may be  
711 gained from published studies on PDC erosion based on field evidence. Following Douillet et al.  
712 (2019) and Pollock et al. (2019), the recumbent flame structures are referred to PDCs of similar  
713 concentration to the undulated structures, and the latter represent an earlier phase of growth of the  
714 recumbent flame structures. Moreover, the recumbent flame structures are a reliable indicator of the  
715 approximate local direction of the currents. Additionally, the recumbent flame structures are related  
716 to conditions of high concentration in the flow boundary zone (Pollock et al., 2019), indicating that  
717 the BT were deposited by mostly concentrated PDCs.

718 By a physical point of view, the undulated (lithofacies ucAL), recumbent flame (lithofacies  
719 rfAL) and rip-up structures (lithofacies ruAL) recognised at the base of BT depositional units are a  
720 signature of instabilities occurring at the boundary of two sheared granular media, and they may  
721 represent the frozen record of granular, pseudo-Kelvin–Helmholtz instabilities. Waves and  
722 overturned stratification like those described at the base of BT are usually the result of simple shear  
723 exerted by the overriding flow on the loose substratum (Allen and Banks, 1972; Mills, 1983;  
724 Valentine et al., 1989; Røe and Hermansen, 2006; Douillet et al., 2015; Pollock et al., 2019). They

725 have been also described in several analogue experimental studies with granular flows over grain  
726 beds (Goldfarb et al., 2002; Mangeney et al., 2010; Rowley et al., 2011; Roche et al., 2013; Farin et  
727 al., 2014).

728 Shear stress  $\tau$  is defined as:

729

$$730 \quad \tau = u_*^2 \rho_{PDC} \quad (2)$$

731

732 where  $u_*$  is the shear velocity, and  $\rho_{PDC}$  is the current density. The minimum velocity needed for  
733 starting bed instability is given by:

734

$$735 \quad u_{*min} = \left[ \frac{g\lambda(1-x^2)}{2\pi x} \right]^{1/2} \quad (3)$$

736

737 where  $g$  is the gravity acceleration,  $\lambda$  is the wavelength of bed instability, and  $x$  the relative flow  
738 concentration ( $\rho_{PDC}/\rho_{bed}$ ) (Douillet et al., 2015). Eq. (3) states that the wavelength of the  
739 instabilities depends on shear velocity and the ratio between particle concentrations of the PDC and  
740 the underlying bed. It is interesting to note that Eq. (3) holds for  $0 \leq x \leq 1$  (Douillet et al., 2015),  
741 which means that instabilities can form only if particle concentration in the bed is greater than that  
742 in the flow. Figure 11 shows that the more diluted the flow is (lower numbers of  $x$ ), the more is the  
743 velocity required to form bed instabilities. In all PDCs the solid-void ratio and flow density ( $\rho_{PDC}$ )  
744 can vary greatly with height, producing flow stratification (e.g., Valentine, 1987; Dellino et al.,  
745 2004), and developing granular flow or fluid-escape dominated flow-boundary zones. The fluid and  
746 solid components abundance and densities determine the physical properties of the flow, which  
747 greatly depend on grain-size distributions and relative abundance of the different solid  
748 componentry. Without direct measurements, a gross estimate of particle concentration and  $\rho_{PDC}$  can  
749 be obtained from the deposits for granular/fluid escape-dominated flows. Assuming a characteristic

750 solid-fluid ratio of 50-60% for ash rich deposits and a mean solid density of  $2400 \text{ kg m}^{-3}$  (e.g.,  
751 Sulpizio et al., 2007; Breard and Lube, 2017; Lube et al. 2019), it results a range of  $\rho_{\text{PDC}}$  of ca.  
752  $1100\text{-}1400 \text{ kg/m}^{-3}$ . Considering that the solid volume fraction can reach 70% in PDC deposits (Gase  
753 et al., 2018) and assuming a flow concentration of 50-60 vol.%, it results in a relative flow  
754 concentration ( $x$ ) of 10-20% lower than the deposit, which can be used to constrain the minimum  
755 shear velocity to form the observed bed instabilities. For wavelength number of 0.16 ( $l=40 \text{ cm}$ ) the  
756 minimum basal shear velocity is less than  $1 \text{ m s}^{-1}$ , while for wavelength number of 0.72 ( $l=450 \text{ cm}$ )  
757 it is less than  $2 \text{ m s}^{-1}$  (Fig. 11), a value comparable to that obtained for the Peach Spring ignimbrite  
758 (Roche et al., 2016). It is to note that the calculated velocities do not reflect velocities at the flow  
759 front, but instead reflect the basal slip velocity at the time of instability formation. The resulting  
760 minimum basal shear stress, which refers the very base of the stratified current (a few mm-cm) may  
761 be calculated in the range of 1-4.5 kPa using Eq. (1).

762

## 763 6. CONCLUSIONS

764

765 A sedimentological analysis of lithofacies, combined with grain-size and componentry  
766 investigation and grain-specific volcanic glass compositional data, for a large number of the different  
767 depositional units of the ash-rich Brown Tuffs (BT) has been carried out on Lipari and Vulcano to  
768 provide constraints on their transport and depositional mechanisms and dispersal area. We rely on the  
769 framework of knowledge acquired so far according to which the BT were generated over a long-time  
770 interval between c. 80 and 6 ka by pulsating hydromagmatic eruptions from eruptive vent(s) inside  
771 the La Fossa caldera on Vulcano. The following are the main outcomes of the present work:

- 772 1. The UBT on Vulcano (24-6 ka) are deposited from ground-hugging ash-rich pyroclastic  
773 density currents (PDCs) that have surmounted the caldera walls. Alternating massive and  
774 planar to cross stratified deposits reflect a repetitive aggradation of PDC pulses  
775 characterised by either fluid escape or granular flow depositional regimes from a fine-



776 grained, concentrated flow-boundary zone (lithofacies mA) or grain by grain deposition  
777 from dilute and turbulent PDCs (lithofacies psA-xsA) during the waning stage of each pulse.

778 2. Intermittently stratified ash deposits of the UBT on Vulcano, with distinctive upwards bends  
779 and pillar- type escape structures through the rupture points are interpreted as the result of  
780 post-depositional disruption of the primary deposits due to fluid escape related to dissipation  
781 of pore pressure between layers at different porosity. This process can be pervasive to  
782 produce almost entirely massive UBT deposits with only fragments of laminae distributed  
783 unevenly as relicts of the original stratified lithofacies.

784 3. Most of the BT on Lipari are emplaced by PDCs that have likely travelled over a narrow  
785 sea inlet. The water density bias produced decoupling of basal denser parts of the currents,  
786 which sunk into the sea, from the turbulent and more diluted upper parts, able to reach  
787 Lipari. This induced selection of particles and accounts for the unusual good sorting and  
788 very fine grain size distribution of BT deposits on Lipari island. Topography-induced  
789 decoupling occurred on Vulcano due to the interaction of southwards laterally spreading  
790 PDCs with the La Fossa Caldera walls. Most of the BT on Lipari and partly on Vulcano  
791 were deposited in fluid escape or granular flow regimes induced by the interaction of the  
792 turbulent parent flows with the paleo-topography, which caused loss of turbulence and  
793 concentration of the solid particles in the flow boundary zone.

794 4. Most of the individual BT depositional units on Lipari (and Vulcano) are characterised at  
795 the base by mixing bands containing pumice, scoria and lithic clasts ripped-up and  
796 embedded from the loose underlying pyroclastic units, as outlined by field study supported  
797 by grain-size and component analyses and geochemical glass investigation of the different  
798 components. These mixing bands indicate erosion and incorporation of loose material from  
799 the underlying beds into the laterally spreading ash flows that deposited the BT. The  
800 recognition of these structures up to the northern sector of Lipari indicates that the PDCs

801 during the BT eruptions travelled up to distances of (at least) 16-17 km from the source area  
802 and possessed a high capacity of impact over the territory.

803 5. Undulated, recumbent flame and rip-up structures are recognised at the base of some BT  
804 depositional units on southern and central Lipari as the result of effective lateral transport  
805 and moderate to high shear stress exerted by the ash flows of the BT to the substratum.  
806 These structures provide indications on the approximate local south-to-north direction of  
807 the currents, and the conditions of high solid concentration of the PDCs that deposited these  
808 BT. Moreover, they can be adopted to estimate a basal shear velocity of the currents of up  
809 to c.  $2 \text{ m s}^{-1}$  and a shear stress in the range of 1-4.5 kPa at the time of structure formation.

810 In conclusion, massive ash deposits of the BT can actually result from the spreading of PDCs that  
811 possess a high erosive power and shear strength at the flow base, representing a substantial hazard  
812 for tens of km away from the source area, which is amplified by the fine grain size that helps  
813 maintaining fluidization and increasing flow mobility.

814

## 815 **ACKNOWLEDGEMENTS**

816 We thank three anonymous reviewers for their thoughtful suggestions to the first draft of this  
817 manuscript, and Catherine Chagué for her kind and careful editing. Sara Meschiari was funded  
818 through a Ph.D. Scholarship of the University of Bologna-Alma Mater Studiorum. Paul G. Albert  
819 was funded through a UKRI Future Leaders Fellowship (MR/S035478/1).

820

## 821 **REFERENCES**

822

823 Albert, P.G., Tomlinson, E.L., Smith, V.C., Di Traglia, F., Pistolesi, M., Morris, A., Donato, P., De  
824 Rosa, R., Sulpizio, R., Keller, J., Rosi, M., Menzies M., 2017. Glass geochemistry of pyroclastic  
825 deposits from the Aeolian Islands in the last 50 ka: a proximal database for tephrochronology.  
826 *Journal of Volcanology and Geothermal Research* 336, 81-107.

- 827 Allen, J.R.L., 1977. The possible mechanics of convolute lamination in graded sand beds. *Journal of*  
828 *the Geological Society London* 134, 19–31.
- 829 Allen, J.R.L., Banks, N.L., 1972. An interpretation and analysis of recumbent folded deformed cross  
830 bedding. *Sedimentology* 19, 257-283.
- 831 Allen, S.R., Cas, R.A.F., 1998. Rhyolitic fallout and pyroclastic density current deposits from a  
832 phreatoplinian eruption in the eastern Aegean Sea, Greece. *Journal of Volcanology and*  
833 *Geothermal Research* 86, 219–251.
- 834 Andrews, B.J., Manga, M., 2012. Experimental study of turbulence, sedimentation, and coignimbrite  
835 mass partitioning in dilute pyroclastic density currents. *Journal of Volcanology and Geothermal*  
836 *Research* 225-226, 30-44.
- 837 Barberi, F., Gasparini, P., Innocenti, F., Ferrara, G., Villari, L., 1973. Volcanism of the southern  
838 Tyrrhenian Sea and its geodynamic implications. *Journal of Geophysical Research* 78, 5221-  
839 5232.
- 840 Beccaluva, L., Gabbianelli, G., Lucchini, F., Rossi, P.L., Savelli, C., 1985. Petrology and K/Ar ages  
841 of volcanics dredged from the Aeolian seamounts: implications for geodynamic evolution of  
842 the Southern Tyrrhenian basin. *Earth and Planetary Science Letters* 74, 187–208.
- 843 Bergeat, A., 1899. Die Äolischen Inseln (Stromboli, Panaria, Salina, Lipari, Vulcano, Filicudi und  
844 Alicudi). *Abhandlungen der Mathematisch-Physikalischen Klasse der Königlich Bayerischen*  
845 *Akademie der Wissenschaften*, vol. 20 I. Abt., München, 274 pp (in German)
- 846 Bernard, J., Kelfoun, K., Le Pennec, J.-L., Vallejo Vargas, S., 2014. Pyroclastic flow erosion and  
847 bulking processes; comparing field-based vs. modeling results at Tungurahua Volcano,  
848 Ecuador. *Bulletin of Volcanology* 76, 1-16.
- 849 Blott, S.J., Pye, K., 2001. GRADISTAT: a grain size distribution and statistics package for the  
850 analysis of unconsolidated sediments. *Earth Surface Processes and Landforms* 26, 1237–  
851 1248.

- 852 Branney, M.J., Kokelaar, P., 2002. Pyroclastic Density Currents and the Sedimentation of  
853 Ignimbrites. Geological Society London Memoirs 27, 143 pp.
- 854 Breard, E.C.P., Lube, G., 2017. Inside pyroclastic density currents—Uncovering the enigmatic flow  
855 structure and transport behaviour in large- scale experiments. Earth and Planetary Science  
856 Letters 458, 22–36.
- 857 Breard, E.C.P., Jones, J.R., Fullard, L., Lube, G., Davies, C., Dufek, J., 2019. The permeability of  
858 volcanic mixtures - Implications for pyroclastic currents. Journal of Geophysical Research,  
859 Solid Earth 124. <https://doi.org/10.1029/2018JB016544>
- 860 Brosch, E., Lube, G., 2020. Spatiotemporal sediment transport and deposition processes in  
861 experimental dilute pyroclastic density currents. Journal of Volcanology and Geothermal  
862 Research 401, 106946. <https://doi.org/10.1016/j.jvolgeores.2020.106946>.
- 863 Cagnoli, B., Romano, G.P., 2010. Effect of grain size on mobility of dry granular flows of angular  
864 rock fragments: An experimental determination. Journal of Volcanology and Geothermal  
865 Research 193, 18–24.
- 866 Calanchi, N., De Rosa, R., Mazzuoli, R., Rossi, P.L., Santacroce, R., Ventura, G., 1993. Silicic  
867 magma entering a basaltic magma chamber: eruptive dynamics and magma mixing – an  
868 example from Salina (Aeolian Islands, southern Tyrrhenian Sea). Bulletin of Volcanology 55,  
869 504–522.
- 870 Cas, R.A.F., Wright, J.V., 1987. Volcanic Successions. Unwin Hyman, London, 528 pp.
- 871 Cas, R.A.F., Wright, H.M.N., Folkes, C.B., Lesti, C., Porreca, M., Giordano, G., Viramonte, J.G.,  
872 2011. The flow dynamics of an extremely large volume pyroclastic flow, the 2.08-Ma Cerro  
873 Galán Ignimbrite, NW Argentina, and comparison with other flow types. Bulletin of  
874 Volcanology 73, 1583–1609.
- 875 Carey, S.N., 1991. Transport and deposition of tephra by pyroclastic flows and surges. SEPM, Society  
876 for Sedimentary Geology, Special Publications 45, 39–57.
- 877 Chappell, J., Shackleton, N.J., 1986. Oxygen isotopes and sea level. Nature 324, 137–140.

- 878 Chiarabba, C., De Gori, P., Speranza, F., 2008. The Southern Tyrrhenian Subduction Zone: deep  
879 geometry, magmatism and Plio-Pleistocene evolution. *Earth and Planetary Science Letters* 268,  
880 408–423.
- 881 Chough, S.K., Sohn, Y.K., 1990. Depositional mechanics and sequences of base surges, Songaksan  
882 tuff ring, Cheju Island, Korea. *Sedimentology* 37, 1115–1135.
- 883 Cicchino, A., Zanella, E., De Astis, G., Lanza, R., Lucchi, F., Tranne, C.A., Airoidi, G., Mana S.,  
884 2011. Rock magnetism and compositional investigation of Brown Tuffs deposits at Lipari and  
885 Vulcano (Aeolian Islands – Italy). *Journal of Volcanology and Geothermal Research* 208, 23-  
886 28.
- 887 Cole, P.D., Guest, J.E., Duncan, A.M., 1993. The emplacement of intermediate volume ignimbrite: a  
888 case study from Roccamonfina volcano, southern Italy. *Bulletin of Volcanology* 55, 467–480.
- 889 Colella, A., Hiscott, R.N., 1997. Pyroclastic surges of the Pleistocene Monte Guardia sequence  
890 (Lipari Island, Italy): depositional processes. *Sedimentology* 44, 47–66.
- 891 Crisci, G.M., De Rosa, R., Lanzafame, G., Mazzuoli, R., Sheridan, M.F., Zuffa, G.G., 1981. Monte  
892 Guardia Sequence: a Late-Pleistocene Eruptive Cycle on Lipari (Italy). *Bulletin of Volcanology*  
893 44, 241-255.
- 894 Crisci, G.M., Delibrias, G., De Rosa, R., Mazzuoli, R., Sheridan, M.F., 1983. Age and petrology of  
895 the Late-Pleistocene Brown Tuffs on Lipari, Italy. *Bulletin of Volcanology* 46, 381-391.
- 896 Crisci, G.M., De Rosa, R., Esperanca, S., Mazzuoli, R., Sonnino, M., 1991. Temporal evolution of a  
897 three component system: the island of Lipari (Aeolian Arc, southern Italy). *Bulletin of*  
898 *Volcanology* 53, 207-221.
- 899 De Astis, G., Dellino, P., De Rosa, R., La Volpe, L., 1997. Eruptive emplacement mechanism of fine  
900 grained pyroclastic deposits widespread on Vulcano Island. *Bulletin of Volcanology* 59, 87-  
901 102.

902 De Astis, G., Ventura, G., Vilardo, G., 2003. Geodynamic significance of the Aeolian volcanism  
903 (Southern Tyrrhenian Sea, Italy) in light of structural, seismological and geochemical data.  
904 *Tectonics* 22, 1040–1057.

905 De Astis, G., Lucchi, F., Dellino, P., La Volpe, L., Tranne, C.A., Frezzotti, M.L., Peccerillo, A., 2013.  
906 Geology, volcanic history and petrology of Vulcano (central Aeolian archipelago). *Geological*  
907 *Society London, Memoirs* 37, 281–348.

908 De Rosa, R., Donato, P., Gioncada, A., Masetti, M., Santacroce, R. 2003. The Monte Guardia eruption  
909 (Lipari, Aeolian Islands): an example of a reversely zoned magma mixing sequence. *Bulletin*  
910 *of Volcanology* 65, 530–543.

911 De Rosa, R., Donato, P., Scarciglia, F., 2016. On the origin and post-depositional history of  
912 widespread massive ash deposits: the case of Intermediate Brown Tuffs (IBT) of Lipari  
913 (Aeolian Islands, Italy). *Journal of Volcanology and Geothermal Research* 327, 135-151.

914 Dellino, P., Isaia, R., Veneruso, M., 2004. Turbulent boundary layer shear flows as an approximation  
915 of base surge at Campi Flegrei (Southern Italy). *Journal of Volcanology and Geothermal*  
916 *Research* 133, 211–228.

917 Dellino, P., Zimanowski, B., Buttner, R., La Volpe, L., Mele, D., Sulpizio, R., 2007. Large-scale  
918 experiments on the mechanics of pyroclastic flow: design, engineering, and first results. *Journal*  
919 *of Geophysical Research* 112, B04202. <https://doi.org/10.1029/2006JB004313>.

920 Dellino, P., Buttner, R., Dioguardi, F., Doronzo, D.M., La Volpe, L., Mele, D., Sonder, I., Sulpizio,  
921 R., Zimanowski, B., 2010. Experimental evidence links volcanic particle characteristics to  
922 pyroclastic flow hazard. *Earth and Planetary Science Letters* 295, 314–320.

923 Dellino, P., De Astis, G., La Volpe, L., Mele, D., Sulpizio, R., 2011. Quantitative hazard assessment  
924 of phreatomagmatic eruptions at Vulcano (Aeolian Islands, Southern Italy), as obtained by  
925 combining stratigraphy, event statistics and physical modelling. *Journal of Volcanology and*  
926 *Geothermal Research* 201, 264-384.

- 927 Dellino, P., Dioguardi, F., Doronzo, D.M., Mele, D., 2019. The rate of sedimentation from turbulent  
928 suspension: An experimental model with application to pyroclastic density currents and  
929 discussion on the grain-size dependence of flow runout. *Sedimentology* 66, 129–145.
- 930 Douillet, G.A., Taisne, B., Tsang-Hin-Sun, M.S.K., Kueppers, U., Dingwell, D.B., 2015. Syn-  
931 eruptive, soft-sediment deformation of deposits from dilute pyroclastic density current: triggers  
932 from granular shear, dynamic pore pressure, ballistic impacts and shock waves. *Solid Earth* 6,  
933 553-572.
- 934 Douillet, G.A., Bernard, B., Bouysson, M., Chaffaut, Q., Dingwell, D.B., Gegg, L., Hoelscher, I.,  
935 Kueppers, U., Mato, C., Ariane Ritz, V., Schlunegger, F., Witting, P., 2019. Pyroclastic dune  
936 bedforms: macroscale structures and lateral variations. Examples from the 2006 pyroclastic  
937 currents at Tungurahua (Ecuador). *Sedimentology* 66, 1531-1559.
- 938 Druitt, T.H., 1998. Pyroclastic density currents. Geological Society London, Special Publications  
939 145, 145–182.
- 940 Druitt, T.H., Avarad, G., Bruni, G., Lettieri, P., Maez, F., 2007. Gas retention in fine-grained  
941 pyroclastic flow materials at high temperatures. *Bulletin of Volcanology* 69, 881-901.
- 942 Dufek, J., Esposti Ongaro, T., Roche, O., 2015. Pyroclastic density currents: processes and models.  
943 In: Sigurdsson, H., Houghton, B., McNutt, S., Rymer, H., Stix, J. (Eds.), *The Encyclopedia of*  
944 *Volcanoes* (second edition). Academic Press, Elsevier, pp. 631–648.
- 945 Ellam, R.M., Menzies, M.A., Hawkesworth, C.J., Leeman, W.P., Rosi, M., Serri, G., 1988. The  
946 transition from calc-alkaline to potassic orogenic magmatism in the Aeolian Islands, Southern  
947 Italy. *Bulletin of Volcanology* 50, 386–398.
- 948 Farin, M., Mangeney, A., Roche, O., 2014. Fundamental changes of granular flow dynamics,  
949 deposition, and erosion processes at high slope angles: insights from laboratory experiments.  
950 *Journal of Geophysical Research-Earth* 119, 504–532.

951 Félix, G., Thomas, N., 2004. Relation between dry granular flow regimes and morphology of  
952 deposits: Formation of levées in pyroclastic deposits. *Earth Planetary and Science Letters* 221,  
953 197-213.

954 Folk RL, Ward WC., 1957. Brazos River bar: a study in the significance of grain size parameters.  
955 *Journal of Sedimentary Petrology* 27, 3–26.

956 Forni, F., Lucchi, F., Peccerillo, A., Tranne, C.A., Rossi, P.L., Frezzotti, M.L., 2013. Stratigraphic  
957 and geological evolution of the Lipari volcanic complex (central Aeolian archipelago).  
958 *Geological Society London Memoirs* 37, 213-279.

959 Francalanci, L., Taylor, S.R., Mcculloch, M.T., Woolhead, J.D., 1993. Geochemical and isotopic  
960 variations in the calc-alkaline rocks of Aeolian arc, southern Tyrrhenian Sea, Italy: constraints  
961 on magma genesis. *Contributions to Mineralogy and Petrology* 113, 300–313.

962 Francalanci, L., Lucchi, F., Keller, J., De Astis, G., Tranne, C.A., 2013. Eruptive, volcano-tectonic  
963 and magmatic history of the Stromboli volcano (north-eastern Aeolian archipelago). *Geological*  
964 *Society London Memoirs* 37, 395–469. Freundt, A., Schmincke, H.U., 1986. Emplacement of  
965 small-volume pyroclastic flows at Lacher See (East Eifel, Germany). *Bulletin of Volcanology*  
966 48, 39–59.

967 Gase, A., Bradford, J.H., Brand, B., 2018. Estimation of porosity and water saturation in dual porosity  
968 pyroclastic deposits from joint analysis of compression, shear, and electromagnetic velocities.  
969 *Geophysics* 83, 1-39.

970 Giaccio, B., Isaia, R., Fedele, F.G., Di Canzio, E., Hoffecker, J., Ronchitelli, A., Sinitsyn, A.A.,  
971 Anikovich, M., Lisitsyn, S.N., Popov, V.V., 2008. The Campanian Ignimbrite and Codola  
972 tephra layers: Two temporal/stratigraphic markers for the Early Upper Palaeolithic in southern  
973 Italy and eastern Europe. *Journal of Volcanology and Geothermal Research* 177, 208–226.

974 Gioncada, A., Mazzuoli, R., Bisson, M., Pareschi, M.T., 2003. Petrology of volcanic products  
975 younger than 42 ka on the Lipari-Vulcano complex (Aeolian Islands, Italy): an example of



976 volcanism controlled by tectonics. *Journal of Volcanology and Geothermal Research* 122, 191–  
977 220.

978 Gioncada, A., Mazzuoli, R., Milton, A.J., 2005. Magma mixing at Lipari (Aeolian Islands, Italy):  
979 insights from textural and compositional features of phenocrysts. *Journal of Volcanology and*  
980 *Geothermal Research* 145, 97–118.

981 Girolami, L., Druitt, T.H., Roche, O., Khrabrykh, Z., 2008. Propagation and hindered settling of  
982 laboratory ash flows. *Journal of Geophysical Research* 113, B02202. [http://dx.doi.org/10.1029/  
983 2007JB005074](http://dx.doi.org/10.1029/2007JB005074).

984 Goldfarb, D.J., Glasser, B.J., Shinbrot, T., 2002. Shear instabilities in granular flows. *Nature* 415,  
985 302–305.

986 Gurioli, L., Cioni, R., Sbrana, A., Zanella, E., 2002. Transport and deposition of pyroclastic density  
987 currents over an inhabited area: the deposits of the AD 79 eruption of Vesuvius at Herculaneum,  
988 Italy. *Sedimentology* 49, 1–26.

989 Hornig-Kjarsgaard, I., Keller, J., Koberski, U., Stadlbauer, E., Francalanci, L., Lenhart, R., 1993.  
990 Geology, stratigraphy and volcanological evolution of the island of Stromboli, Aeolian arc,  
991 Italy. *Acta Vulcanologica* 3, 21–68.

992 Keller, J., 1967. Alter und Abfolge der vulkanischen Ereignisse auf den Aolischen Inseln. *Berichte*  
993 *der Naturforschenden Gesellschaft zu Freiburg i. Br.* 57, 33–67 (in German).

994 Keller, J., 1980a. The island of Salina. *Rendiconti della Società Italiana di Mineralogia e Petrologia*  
995 36, 489-524.

996 Keller, J., 1980b. The Island of Vulcano. *Rendiconti della Società Italiana di Mineralogia e Petrologia*  
997 36, 369-414.

998 Keller, J., Ryan, W.B.F., Ninkovich, D., Altherr, R., 1978. Explosive volcanic activity in the  
999 Mediterranean over the past 200 000 yr as recorded in deep-sea sediments. *Geological Society*  
1000 *of America Bulletin* 89, 591–604.

- 1001 LaBerge, R.D., Giordano, G., Cas, R.A.F., Ailleres, L., 2006. Syn-depositional substrate deformation  
1002 produced by the shear force of a pyroclastic density current: An example from the Pleistocene  
1003 ignimbrite at Monte Cimino, northern Lazio, Italy. *Journal of Volcanology and Geothermal*  
1004 *Research* 158, 307–320.
- 1005 Leocat, E., 2011. Histoire Eruptive des Volcans du Secteur Occidental des Iles Eoliennes (Sud de la  
1006 Mer Tyrrhenienne, Italie) (Ph.D. thesis). University of Paris 11, Orsay (in French and English).
- 1007 Losito, R., 1989. Stratigrafia, Caratteri Deposizionali e Aree Sorgente dei Tufi Bruni delle Isole Eolie  
1008 (Ph.D. thesis). University of Bari, Italy (in Italian).
- 1009 Lowe, D.R., 1982. Sediment gravity flows: II. Depositional models with special references to deposits  
1010 of high-density turbidity currents. *Journal of Sedimentary Petrology* 52, 279–297.
- 1011 Lube, G., Cronin, S.J., Platz, T., Freundt, A., Procter, J.N., Henderson, C., Sheridan, M.F., 2007.  
1012 Flow and deposition of pyroclastic granular flows: a type example from the 1975 Ngauruhoe  
1013 eruption, New Zealand. *Journal of Volcanology and Geothermal Research* 161, 165–186.
- 1014 Lube, G., Breard, E.C.P., Jones, J., Fullard, L., Dufek, J., Cronin, S.J., Wang, T., 2019. Generation  
1015 of air lubrication within pyroclastic density currents. *Nature Geoscience* 12, 381–386.
- 1016 Lube, G., Breard, E.C.P., Esposti-Ongaro, T., Dufek, J., Brand, B., 2020. Multiphase flow behaviour  
1017 and hazard prediction of pyroclastic density currents. *Nature Reviews Earth & Environment* 1,  
1018 348–365.
- 1019 Lucchi, F., 2009. Late-Quaternary marine terrace deposits as tools for wide-scale correlation of  
1020 unconformity-bounded units in the volcanic Aeolian archipelago (southern Italy). *Sedimentary*  
1021 *Geology* 216, 158–178.
- 1022 Lucchi, F., 2013. Stratigraphic methodology for the geological mapping of volcanic areas: insights  
1023 from the Aeolian archipelago (southern Italy). *Geological Society London Memoirs* 37, 37–55.
- 1024 Lucchi, F., Tranne, C.A. Calanchi, N., Pirazzoli, P.A., Romagnoli, C., Radtke, U., Reyss, J.L., Rossi,  
1025 P.L., 2004. Stratigraphic constraints to date late-Quaternary ancient shorelines and to evaluate  
1026 vertical movements at Lipari (Aeolian Islands). *Quaternary International* 115/116, 105–115.

- 1027 Lucchi, F., Tranne, C.A., De Astis, G., Keller, J., Losito, R., Morche, W., 2008. Stratigraphy and  
1028 significance of Brown Tuffs on the Aeolian Islands (southern Italy). *Journal of Volcanology*  
1029 and *Geothermal Research* 177, 49-70.
- 1030 Lucchi, F., Gertisser, R., Keller, J., Forni, F., De Astis, G., Tranne, C.A., 2013a. Eruptive history and  
1031 magmatic evolution of the island of Salina (central Aeolian archipelago). *Geological Society*  
1032 *London Memoirs* 37, 155-211.
- 1033 Lucchi, F., Keller, J., Tranne, C., 2013b. Regional stratigraphic correlations across the Aeolian  
1034 archipelago (southern Italy). *Geological Society London Memoirs* 37, 55-81.
- 1035 Lucchi, F., Tranne, C.A., Peccerillo, A., Keller, J., Rossi, P.L., 2013c. Geological history of the  
1036 Panarea volcanic group (eastern Aeolian archipelago). *Geological Society London Memoirs* 37,  
1037 349-393.
- 1038 Lucchi, F., Peccerillo, A., Tranne, C.A., Rossi, P.L., Frezzotti, M.L., Donati, C., 2013d. Volcanism,  
1039 calderas, and magmas of the Alicudi composite volcano (western Aeolian archipelago).  
1040 *Geological Society London Memoirs* 37, 83–111.
- 1041 Lucchi, F., Santo, A.P., Tranne, C.A., Peccerillo, A., Keller, J., 2013e. Volcanism, magmatism,  
1042 volcano-tectonics and sea-level fluctuations in the geological history of Filicudi (western  
1043 Aeolian archipelago). *Geological Society London Memoirs* 37, 113-153.
- 1044 Mangeney, A., Roche, O., Hungr, O., Mangold, N., Faccanoni, G., Lucas, A., 2010. Erosion and  
1045 mobility in granular collapse over sloping beds, *Journal of Geophysical Research-Earth* 115,  
1046 F03040. <https://doi.org/10.1029/2009JF001462>.
- 1047 Manetti, P., Pasquaré, G., Tibaldi, A., Tsegaye, A., 1988. Geology of the island of Filicudi (Aeolian  
1048 arc). *Bollettino G.N.V. (Gruppo Nazionale di Vulcanologia, Italia)* IV, 368-382.
- 1049 Manetti, P., Pasquaré, G., Tibaldi, A., Tsegaye, A., 1995. A new geo-vulcanological map of Filicudi  
1050 island (Aeolian arc, Italy). *Acta Vulcanologica* 7, 1-5.

- 1051 Mathisen, M.E., Vondra, C.F., 1983. The fluvial and pyroclastic deposits of the Cagayan basin,  
1052 Northern Luzon, Philippines—an example of non-marine volcanoclastic sedimentation in an  
1053 interarc basin. *Sedimentology* 30, 369–392.
- 1054 Mele, D., Dioguardi, F., Dellino, P., Isaia, R., Sulpizio, R., Braia, G., 2015. Hazard of pyroclastic  
1055 density currents at the Campi Flegrei Caldera (Southern Italy) as deduced from the combined  
1056 use of facies architecture, physical modeling and statistics of the impact parameters. *Journal of*  
1057 *Volcanology and Geothermal Research* 299, 35–53.
- 1058 Meschiari, S., Albert, P.G., Lucchi, F., Sulpizio, R., Smith, V.C., Kearne, R., Tranne, C.A., 2020.  
1059 Frequent activity on Vulcano (Italy) spanning the last 80 ky: New insights from the chemo-  
1060 stratigraphy of the Brown Tuffs. *Journal of Volcanology and Geothermal Research* 406.  
1061 <https://doi.org/10.1016/j.jvolgeores.2020.107079>.
- 1062 Miall, A.D., 1978. Lithofacies types and vertical profiles models in braided river deposits: a summary.  
1063 In: Miall, A.D. (Ed.), *Fluvial Sedimentology*. Canadian Society of Petroleum Geologists,  
1064 *Memoirs* 5, 597–604.
- 1065 Miall, A.D., 1985. Architectural-element analyses: a new method of facies analyses applied to fluvial  
1066 deposits. *Earth-Science Reviews* 22, 261–308.
- 1067 Mills, P.C., 1983. Genesis and diagnostic value of soft-sediment deformation structures: a review.  
1068 *Sedimentary Geology* 35, 83–104.
- 1069 Morche, W., 1988. *Tephrochronologie der Aolischen Inseln* (Ph.D. thesis). Albert-Ludwigs-  
1070 *Universität Freiburg, Germany* (in German).
- 1071 Nichols, R., Sparks, R., and Wilson, C., 1994. Experimental studies of the fluidization of layered  
1072 sediments and the formation of fluid escape structures. *Sedimentology* 41, 233–253.
- 1073 Odonne, F., Callot, P., Debrouas, E.-J., Sempere, T., Hoareau, G., and Maillard, A., 2011. Soft-  
1074 sediment deformation from submarine sliding: Favourable conditions and triggering  
1075 mechanisms in examples from the Eocene Sobrarbe delta (Ainsa, Spanish Pyrenees) and the  
1076 mid-Cretaceous Ayabacas Formation (Andes of Peru). *Sedimentary Geology* 235, 234–248.

- 1077 Owen, G., 1987. Deformation processes in unconsolidated sands. Geological Society London, Special  
1078 Publications 29, 11–24.
- 1079 Peccerillo, A., De Astis, G., Faraone, D., Forni, F., Frezzotti, M.L., 2013. Compositional variations  
1080 of magmas in the Aeolian arc: implications for petrogenesis and geodynamics. Geological  
1081 Society London, Memoirs 37, 489–508.
- 1082 Pichler, H., 1980. The Island of Lipari. Rendiconti della Società Italiana di Mineralogia e Petrologia  
1083 36, 415-440.
- 1084 Pollock, N.M., Brand, B.D., Rowley, P.J., Sarocchi, D., Sulpizio, R., 2019. Inferring pyroclastic  
1085 density current flow conditions using syn-depositional sedimentary structures. Bulletin of  
1086 Volcanology 81, 46. <http://dx.doi.org/10.1007/s00445-019-1303-z>
- 1087 Kowalczuk, P.B., Drzymala, J., 2016. Physical meaning of the Sauter mean diameter of spherical  
1088 particulate matter. Particulate Science and Technology 34, 645-647.
- 1089 Roche, O., 2015. Nature and velocity of pyroclastic density currents inferred from models of  
1090 entrainment of substrate lithic clasts. Earth Planetary and Science Letters 418, 115-125.
- 1091 Roche, O., Montserrat, S., Niño, Y., Tamburrino, A., 2008. Experimental observations of water-like  
1092 behaviour of initially fluidized, unsteady dense granular flows and their relevance for the  
1093 propagation of pyroclastic flows. Journal of Geophysical Research 113, B12203.  
1094 <http://dx.doi.org/10.1029/2008JB005664>.
- 1095 Roche, O., Niño, Y., Mangeney, A., Brand, B.D., Pollock, N.M., Valentine, G.A., 2013. Dynamic  
1096 pore-pressure variations induce substrate erosion by pyroclastic flows. Geology 41, 1107–1110.
- 1097 Roche, O., Buesch, D.C., Valentine, G.A., 2016. Slow-moving and far-travelled dense pyroclastic  
1098 flows during the Peach Spring super-eruption. Nature Communications 7, 10890. doi:  
1099 10.1038/ncomms10890
- 1100 Roche, O., Azzaoui, N., Guillin, A., 2021. Discharge rate of explosive volcanic eruption controls  
1101 runout distance of pyroclastic density currents. Earth and Planetary Science Letters 568,  
1102 117017. <https://doi.org/10.1016/j.epsl.2021.117017>

- 1103 Røe, S.-L., Hermansen, M., 2006. New aspects of deformed cross-strata in fluvial sandstones:  
1104 examples from Neoproterozoic formations in northern Norway. *Sedimentary Geology* 186,  
1105 283–293.
- 1106 Rohling, E.J., Foster, G.L., Grant, K.M., Marino, G., Roberts, A.P., Tamisiea, M.E., Williams, F.,  
1107 2014. Sea-level and deep-sea-temperature variability over the past 5.3 million years. *Nature*  
1108 508, 477–482.
- 1109 Rowley, P.J., Kokelaar, P., Menzies, M., Waltham, D., 2011. Shear derived mixing in dense granular  
1110 flows. *Journal of Sedimentary Research* 81, 874–884.
- 1111 Sauter, J., 1926. Die Grössenbestimmung der in Gemischnebeln von Verbrennungskraftmaschinen  
1112 vorhandenen Brennstoffteilchen. VDI-Verlag, Berlin, Forschungsarbeiten auf dem Gebiete des  
1113 Ingenieurwesens, 279 pp (in German).
- 1114 Selker, J.S., 1993. Expressions for the formation of load casts in soft sediment. *Journal of*  
1115 *Sedimentary Research* 63, 1149–1151.
- 1116 Smith, G.A., 1986. Coarse-grained nonmarine volcanoclastic sediment: terminology and depositional  
1117 process. *Geological Society of America Bulletin* 97, 1–10.
- 1118 Smith, G.A., 1987. The influence of explosive volcanism on fluvial sedimentation: the Deschutes  
1119 formation (Neogene) in central Oregon. *Journal of Sedimentary Petrology* 57, 613–629.
- 1120 Smith, G.M., Williams, R., Rowley, P.J., Parsons, P.D., 2018. Investigation of variable aeration of  
1121 monodisperse mixtures: implications for pyroclastic density currents. *Bulletin of Volcanology*  
1122 80, 67. <https://doi.org/10.1007/s00445-018-1241-1>
- 1123 Sohn, Y.K., Chough, S.K., 1989. Depositional processes of the Suwolbong Tuff Ring, Cheju Island  
1124 (Korea). *Sedimentology* 36, 837–855.
- 1125 Sohn, Y.K., 1997. On traction carpet sedimentation. *Journal of Sedimentary Research* 67, 502–509.  
1126
- 1127 Sulpizio, R., Dellino, P., 2008. Sedimentology, depositional mechanisms and pulsating behaviour of  
1128 pyroclastic density currents. *Developments in Volcanology* 10, 57–96.

- 1129 Sulpizio, R., Mele, D., Dellino, P., La Volpe, L., 2007. Deposits and physical properties of pyroclastic  
1130 density currents during complex Subplinian eruptions: the AD 472 (Pollena) eruption of  
1131 Somma-Vesuvius, Italy. *Sedimentology* 54, 607–635.
- 1132 Sulpizio, R., De Rosa, R., Donato, P., 2008a. The influence of variable topography on the depositional  
1133 behaviour of pyroclastic density currents: the examples of the Upper Pollara eruption (The  
1134 island of Salina, southern Italy). *Journal of Volcanology and Geothermal Research* 175, 367–  
1135 385.
- 1136 Sulpizio, R., Bonasia, R., Dellino, P., Di Vito, M.A., La Volpe, L., Mele, D., Zanchetta, G., Sadori,  
1137 L., 2008b. Discriminating the-long distance dispersal of fine ash from sustained columns or  
1138 near ground ash clouds: the example of the Pomici di Avellino eruption (Somma-Vesuvius,  
1139 Italy). *Journal of Volcanology and Geothermal Research*, 177, 263-276. [doi:  
1140 10.1016/j.jvolgeores.2007.11.012](https://doi.org/10.1016/j.jvolgeores.2007.11.012)
- 1141 Sulpizio, R., Bonasia, R., Dellino, P., Mele, D., Di Vito, M.A., La Volpe, L., 2010. The Pomici di  
1142 Avellino eruption of Somma-Vesuvius (3.9 ka BP). Part II: Sedimentology and physical  
1143 volcanology of pyroclastic density current deposits. *Bulletin of Volcanology* 72, 559–577.
- 1144 Sulpizio, R., Alçiçek, M.C., Zanchetta, G., Solari, L., 2013. Recognition of the Minoan tephra in  
1145 Acigöl Basin, Western Turkey: implications for inter archive correlations and fine ash dispe.  
1146 *Journal of Quaternary Science*, 28, 329-336.
- 1147 Sulpizio, R., Dellino, P., Doronzo, D.M., Sarocchi D., 2014. Pyroclastic density currents: state of the  
1148 art and perspectives. *Journal of Volcanology and Geothermal Research* 283, 36–65.
- 1149 Sulpizio, R., Castioni, D., Rodriguez-Sedano, L.A., Sarocchi, D., Lucchi, F., 2016. The influence of  
1150 slope-angle ratio on the dynamics of granular flows: insights from laboratory experiments.  
1151 *Bulletin of Volcanology* 78, 77. <https://doi.org/10.1007/s00445-016-1069-5>
- 1152 Tomlinson, E.L., Albert, P.G., Wulf, S., Brown, R., Smith, V.C., Keller, J., Orsi, G., Bourne, A.J.,  
1153 Menzies, M.A., 2014. Age and geochemistry of tephra layers from Ischia, Italy: constraints

1154 from proximal-distal correlations with Lago Grande di Monticchio. *Journal of Volcanology and*  
1155 *Geothermal Research* 287, 22-39.

1156 Valentine, G.A., 1987. Stratified flow in pyroclastic surges. *Bulletin of Volcanology* 49, 616–630.

1157 Valentine, G.A., Buesch, D.C., Fisher, R.V., 1989. Basal layered deposits of the Peach Springs Tuff,  
1158 northwestern Arizona, USA. *Bulletin of Volcanology* 51, 395–414.

1159 Ventura, G., 2013. Kinematics of the Aeolian volcanism (Southern Tyrrhenian Sea) from geophysical  
1160 and geological data. *Geological Society London, Memoirs* 37, 3–11.

1161 Waelbroeck, C., Labeyrie, L., Michel, E., Duplessy, J.C., McManus, J.F., Lambeck, K., Balbon, E.,  
1162 Labracherie, M., 2002. Sea-level and deep water temperature changes derived from  
1163 foraminifera isotopic records. *Quaternary Science Reviews* 21, 295–305.

1164 Waresback, D.B., Turbeville, B.N., 1990. Evolution of a Plio-Pleistocene volcanogenic alluvial fan:  
1165 the Puye formation, Jemez Mountains, New Mexico. *Geological Society America Bulletin* 102,  
1166 298–314.

1167

1168 **TABLES**

1169

1170 **Tab. 1.** Selected outcrops, stratigraphy and measurements of the sin-depositional sedimentary  
1171 structures. The distance from the source area is arbitrarily measured relative to the centre of the La  
1172 Fossa Caldera. The sample names refer to the BT depositional units selected for chemical analyses.  
1173 Labels for the sedimentary structures: MB=mixing band; US=undulated structure; FS=recumbent  
1174 flame structure; RS=rip-up structure. In the column of sedimentary structures, the symbol / indicates  
1175 that there is no direct evidence in the field of mixed lithofacies, but the process of clast-embedding is  
1176 outlined by means of geochemical analyses.

1177

1178 **Tab. 2.** Lithofacies codes, description and interpretation of the lithofacies recognised in the BT  
1179 investigated in the present work. The first letters of the lithofacies code indicate the general



1180 appearance of the deposit (m = massive, ps = planar stratified, xs = cross-stratified, is = intermittently  
1181 stratified, etc.) and the capital letters indicate the grain size (A = ash, L = lapilli).

1182

1183 **Tab. 3.** Grain size statistical parameters of Folk and Ward (1957) for the different sub-populations  
1184 recognised in the samples from the base of some BT depositional units: BT=Brown Tuffs; mg=Monte  
1185 Guardia unit; lpt=Lower Pollara Tuffs; fa=Falcone unit. The parameters by Folk and Ward (1957)  
1186 were calculated by means of the GRADISTAT program (Blott and Pye, 2001). The Sauter mean  
1187 diameter (Sauter 1926) of the different BT sub-populations is estimated using the method of Breard  
1188 et al. (2019).

1189

## 1190 **FIGURES**

1191

1192 **Fig. 1.** Sketch maps of the islands of Vulcano and Lipari (A) showing the areal distribution of the BT  
1193 deposits and the location of outcrops where the sedimentary structures object of the present study  
1194 have been observed (L1-13, V1-6). The inset (B) shows the location of the Aeolian Islands and  
1195 seamounts in the southern Tyrrhenian sea (depth contour lines in metres below sea level). Coordinates  
1196 conform to the Gauss-Boaga System (IGM). In (C) there is a sketch chronostratigraphic framework  
1197 showing the development of Aeolian subaerial volcanism and the time-stratigraphic interval of BT  
1198 deposition. Labels for the main tephra layers are: pt = Petrazza Tuffs; gpt = Grey Porri Tuffs; it =  
1199 Ischia Tephra; lpt = Lower Pollara Tuffs; gu = Monte Guardia pumice; vg = Vallone del Gabellotto  
1200 pumice; pn = Punte Nere tuffs. References: Alicudi = Lucchi et al. (2013c); Filicudi = Lucchi et al.  
1201 (2013d); Salina = Lucchi et al. (2013a); Lipari = Forni et al. (2013); Panarea = Lucchi et al. (2013b);  
1202 Vulcano = De Astis et al. (2013); Stromboli = Francalanci et al. (2013).

1203

1204 **Fig. 2.** Generalized stratigraphic succession of the BT derived from correlations between the islands  
1205 of Lipari and Vulcano. The BT succession is subdivided into (at least) 16 depositional units (BT1-

1206 16) superposed to the LBT, IBT, IBT-upper and UBT macro-units by means of interlayered volcanic  
1207 units and tephra layers, erosive surfaces and reworked horizons (see also Meschiari et al., 2020). The  
1208 individual depositional units of the UBT on Vulcano have a different name because they cannot be  
1209 directly correlated with those on Lipari. References for the stratigraphy of the two islands are: Forni  
1210 et al., 2013 (Lipari); De Astis et al., 2013 (Vulcano). The stratigraphic units interlayered within the  
1211 BT that are characterised by the sedimentary structures object of this work are described in Table 1.

1212

1213 **Fig. 3.** Outcrop photographs of the BT and their distinctive lithofacies. A) Massive deposits  
1214 (lithofacies mA) of the BT on Lipari (outcrop L5). The BT in this outcrop correspond to the IBT-  
1215 upper and UBT macro-units developed above the Monte Guardia marker bed. B) UBT deposits on  
1216 Vulcano (outcrop V1) characterised by planar to cross-stratified lithofacies (psA-xsA). C) Alternating  
1217 massive (mA) and intermittently stratified (isA) lithofacies of the UBT on Vulcano (outcrop V3). D)  
1218 Detailed view of the deposits of Figure 3C. E) Detail of the ruptured laminae of the intermittently  
1219 stratified deposits of UBT. The arrows indicate distinctive upward bending of the laminae in the  
1220 rupture points. F) Intermittently stratified ash (isA) deposits of the UBT on Vulcano (outcrop V2).  
1221 G) Close view of the deposits of Figure 3G showing ruptured laminae with typical upward  
1222 deformation and columns of coarse ash (arrow) and inflated deformation of the laminae before the  
1223 rupture (\*). H) Close view of the deposits of Figure 3G showing ruptured laminae with typical upward  
1224 deformation (arrow). I) Massive deposits of the UBT on Vulcano near to Grotta dei Pisani that contain  
1225 fragments of laminae (arrows) representing relicts of the stratified lithofacies.

1226

1227 **Fig. 4.** Field evidence of the mixing bands recognised at base of different BT depositional units on  
1228 Lipari and Vulcano, shown in stratigraphic order (starting from the oldest) according to Fig. 2. A)  
1229 Vallone dei Lacci, Lipari (outcrop L8): mixing band (\*) between the BT4 depositional unit and the  
1230 Grey Porri Tuffs (gpt). B) Valle Muria, Lipari (outcrop L2): mixing band (\*) between the BT8  
1231 depositional unit and the Punta del Perciato pumice (pe). C) Mixing band (\*) between the BT9

1232 depositional unit and the Falcone pumice (pe) at Valle Muria, Lipari (outcrop L2). D) Detail of the  
1233 mixing band in Figure 4C. E) Spiaggia Valle Muria, Lipari (outcrop L1): mixing band (\*) between  
1234 the BT9 depositional unit and the Falcone pumice (pe). F) Valle Muria, Lipari (outcrop L2): scattered  
1235 pumice lapilli of the Falcone unit (fa) embedded within the overlying BT9 depositional unit. G) Gelso,  
1236 Vulcano (outcrop V5): mixing band (\*) between the BT12 depositional unit and the Monte Guardia  
1237 tephra layer (gu). H) Passo del Piano, Vulcano (outcrop V1): mixing band (\*) between the BT16(V)  
1238 depositional unit and the Vallone del Gabellotto pumice (vg).

1239

1240 **Fig. 5.** Field evidence of shear structures on Lipari. A) Tunnel Canneto, Lipari (outcrop L5):  
1241 undulated structure (lithofacies ucAL) along the contact between the BT12 depositional unit and the  
1242 underlying Monte Guardia pumice succession. B) Crest of the undulated structure of Figure 5A. In  
1243 the inset it is shown a zoom on the crest of the undulated structure made up of mixed material between  
1244 the BT12 and the underlying incoherent pyroclastic deposit. C) Spiaggia Valle Muria, Lipari (outcrop  
1245 L1): panoramic view of the undulated structure (lithofacies ucAL) along the contact between the BT9  
1246 depositional unit and the underlying Falcone pumice succession. D) Trail of pumice and lithic lapilli  
1247 of the Falcone pumice succession embedded within the overlying BT9 depositional unit (see C for  
1248 location), representing the tail of a recumbent flame structure (lithofacies rfAL). E) Deformed bed of  
1249 mixed material between the BT9 depositional unit and pumice lapilli from the underlying Falcone  
1250 succession, representing the trunk of a not fully developed recumbent flame structure (lithofacies  
1251 rfAL). F) Detail of the undulated contact in Figure 5C showing a hook-like structure of rip-up lapilli  
1252 from the underlying Falcone unit (lithofacies ruAL).

1253

1254 **Fig. 6.** Grain-size and components frequency histograms of weight % at half-phi intervals and pie  
1255 charts of the components of representative samples of the mixing bands at the base of distinct BT  
1256 depositional units in outcrops L2, L5, L10 and L12 on Lipari (see Fig. 1A for location).

1257 Representative photographs of the outcrops are also shown. The outcrops are displayed relative to an  
1258 increasing distance from the inferred source area of La Fossa Caldera on Vulcano from base to top.

1259

1260 **Fig. 7.** TAS (A) and  $K_2O/SiO_2$  (B) classification diagrams of the BT glasses compared to the volcanic  
1261 glasses of explosive eruption deposits produced on Vulcano, Lipari and Salina during the last 50 ky.  
1262 Data for the BT glasses are from Meschiari et al. (2020), whilst the data for Vulcano, Lipari and  
1263 Salina are from Albert et al. (2017). Error bars represent 2\*standard deviations of replicated analyses  
1264 of the StHs6/80-G secondary standard glass run alongside the BT samples. The secondary  
1265 components recognised in distinct BT depositional units referred to the LBT, IBT, IBT-upper and  
1266 UBT macro-units are compared to the compositions of the underlying proximal pyroclastic units in  
1267 distinct major element glass geochemical variation diagrams (A-N). The stratigraphic succession of  
1268 BT depositional units (BT3, BT4, BT8, BT9, BT10, BT12, BT14-V, BT16-V) refers to Fig. 2. Data  
1269 for the BT glasses are from Meschiari et al. (2020). References for the pyroclastic units used for  
1270 comparison are: Grey Porri Tuffs (w.r.) = Sulpizio et al. (2016); Grey Porri Tuffs, Salina, proximal =  
1271 Albert et al. (2017); Grey Porri Tuffs, Lipari medial, Vulcano medial-distal and Panarea, distal =  
1272 Sulpizio et al., 2016; Meschiari et al. (2020); Lip1 = Meschiari et al. (2020); Falcone = Albert et al.  
1273 (2017); Punta del Perciato = Albert et al. (2017); Monte Guardia field = Albert et al. (2017) and  
1274 Meschiari et al. (2020); Monte Guardia (1) = Albert et al. (2017); Monte Guardia (2) = Meschiari et  
1275 al. (2020); Cugni di Molinello = Meschiari et al. (2020); Vallone del Gabellotto (1) = Albert et al.  
1276 (2017); Vallone del Gabellotto (2) = Meschiari et al. (2020).

1277

1278 **Fig. 8.** Sketch of the transport and depositional behaviour of the PDCs during the UBT eruptions on  
1279 Vulcano island when interacting with the La Fossa Caldera wall (arrows indicate the flow  
1280 direction). In the inset, a model explaining the formation of lithofacies altpsmA (alternance of  
1281 planar stratified and massive ash) as continuous aggradation of deposits from different PDC pulses  
1282 (a, b, c, d) in the area of il Piano to the south of the source area, and the lithofacies isA

1283 (intermittently stratified ash) as disruption of the deposits due to fluid escape (d, e, f). Not to scale.

1284

1285 **Fig. 9.** Sketch of the formation of syn-depositional sedimentary structures (mixing bands, undulated  
1286 structures and recumbent flame structures) at the base of the BT deposits as the result of lateral  
1287 transport and high shear stress exerted by the PDCs of the BT on the loose underlying pyroclastic  
1288 (pumice) material along downslope and upslope paths on the island of Lipari, to the north of the La  
1289 Fossa Caldera source area. Arrows indicate the flow direction. Not to scale.

1290

1291 **Fig. 10.** Sketch of the transport and depositional behaviour of the BT PDCs laterally spreading from  
1292 the La Fossa caldera source on Vulcano towards the island of Lipari, crossing the narrow sea arm of  
1293 the Bocche di Vulcano and interacting with the irregular paleo-topography of Lipari (see  
1294 explanation in the text).

1295

1296 **Fig. 11.** Diagrams showing variations of minimum basal shear velocity ( $u_*$ ) vs. relative flow  
1297 concentration between PDCs and an underlying bed ( $x = \rho_{PDC} / \rho_{bed}$ ) for different wavelength numbers  
1298 ( $\lambda/2\pi$ ) of basal instabilities. Dashed lines indicate the minimum basal shear velocity for the observed  
1299 wavelength of undulated structures of 40 cm ( $\lambda/2\pi=0.16$ ) and 450 cm ( $\lambda/2\pi=0.72$ ) as example of bed  
1300 instabilities in the case study of the BT eruptions.

1301

## 1302 **SUPPLEMENTARY MATERIAL**

1303

1304 **Supplementary File 1** - Main characteristics of tephra units used for the subdivisions of the BT  
1305 succession and showing evidence of syn-depositional clast incorporation within distinct BT  
1306 depositional units (listed in stratigraphic order starting from the older one). Chemical composition of  
1307 juvenile glass fragments (w.r=whole rock) and mineralogy are reported by referring to: (1) present  
1308 work; (2) Meschiari et al. (2020); (3) Albert et al (2017); (4) Sulpizio et al. (2016); (5) Tomlinson et

1309 al. (2014); (6) De Astis et al (2013); (7) Gioncada et al. (2005); (8) De Rosa et al. (2003); (9) Calanchi  
1310 et al. (1993). Labels for compositions: CA=calcalkaline, HKCA=high-k calcalkaline,  
1311 SHO=shoshonite series; Bas-And=basaltic andesite, And=andesite, Dac=dacite, Rhy=rhyolite,  
1312 Sho=shoshonite. Labels for phenocrysts: pl=plagioclase, kf=K-feldspar; cpx=clinopyroxene;  
1313 opx=orthopyroxene, bt=biotite; ol=olivine; amp=amphibole; ox=oxides; ap=apatite; zr=zircon;  
1314 ti=titanite; acm=acmite). Proximal stratigraphic units refer to: (1) Lucchi et al. (2008); (2) Forni et al.  
1315 (2013); (3) Lucchi et al. (2013a); (4) De Astis et al. (2013). Age references: (1) Morche (1988); (2)  
1316 Soligo et al. (2000); (3) Siani et al. (2004); (4) Leocat (2011); (5) Lucchi et al. (2013a; 2013b); (6)  
1317 Sulpizio et al. (2016); (7) Giaccio et al. (2017); (8) Meschiari et al. (2020).

1318

1319 **Supplementary File 2** - Representative major and minor element compositions of samples relative  
1320 to the mixing bands recognised in this study at the base of different Brown Tuffs (BT) units, according  
1321 to LBT, IBT, IBT-upper and UBT macro-units. Totals are pre-normalised analytical totals. For each  
1322 of the samples, we include representative analyses for the main BT juvenile component and the  
1323 secondary components (sec. comp.) relative to the process of clast embedding from the underlying  
1324 pyroclastic units. Representative analyses for the proximal pyroclastic units used for the correlation  
1325 of the secondary components are reported for comparison (in grey): gpt=Grey Porri Tuffs, Salina;  
1326 pe=Punta del Perciato, Lipari; fa=Falcone, Lipari; Lip1 tephra layer, Lipari; mg=Monte Guardia,  
1327 Lipari; cm=Cugni di Molinello, Vulcano; vg=Vallone del Gabellotto, Lipari. Compositions of the  
1328 proximal pyroclastic units and the BT conform to Meschiari et al. (2020), except for "pe", "fa" and  
1329 "mg" which are from Albert et al. (2017).

1330

## **Highlights**

- Sedimentological analysis of widespread ash-rich pyroclastic deposits
- Deposits from ground-hugging pulsating pyroclastic density currents (PDCs)
- Post-depositional disruption due to fluid escape and dissipation of pore pressure
- Erosion and clast embedding by PDCs at several kms away from the source area
- Shear-related granular instability structures at the base of PDC deposits

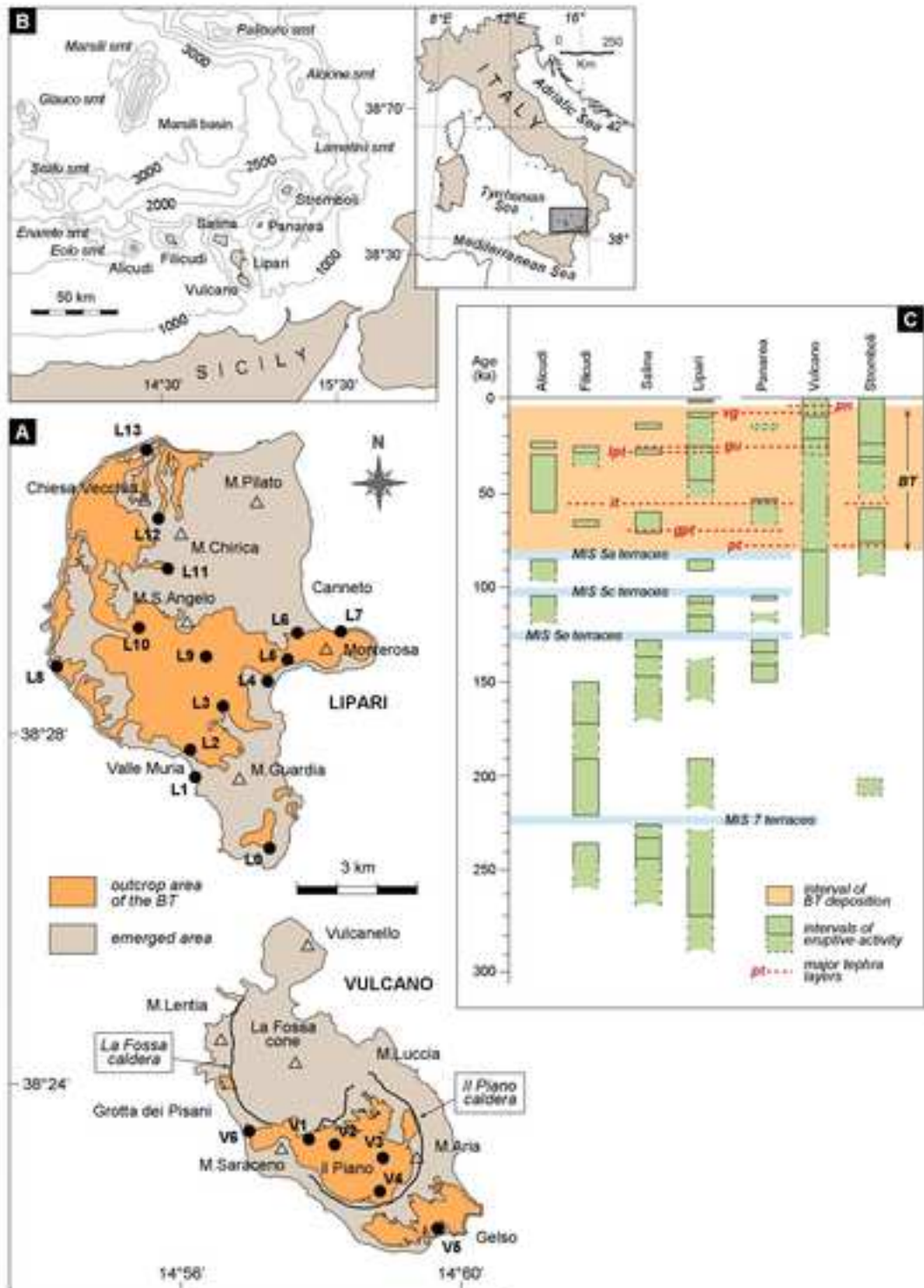


Fig. 1



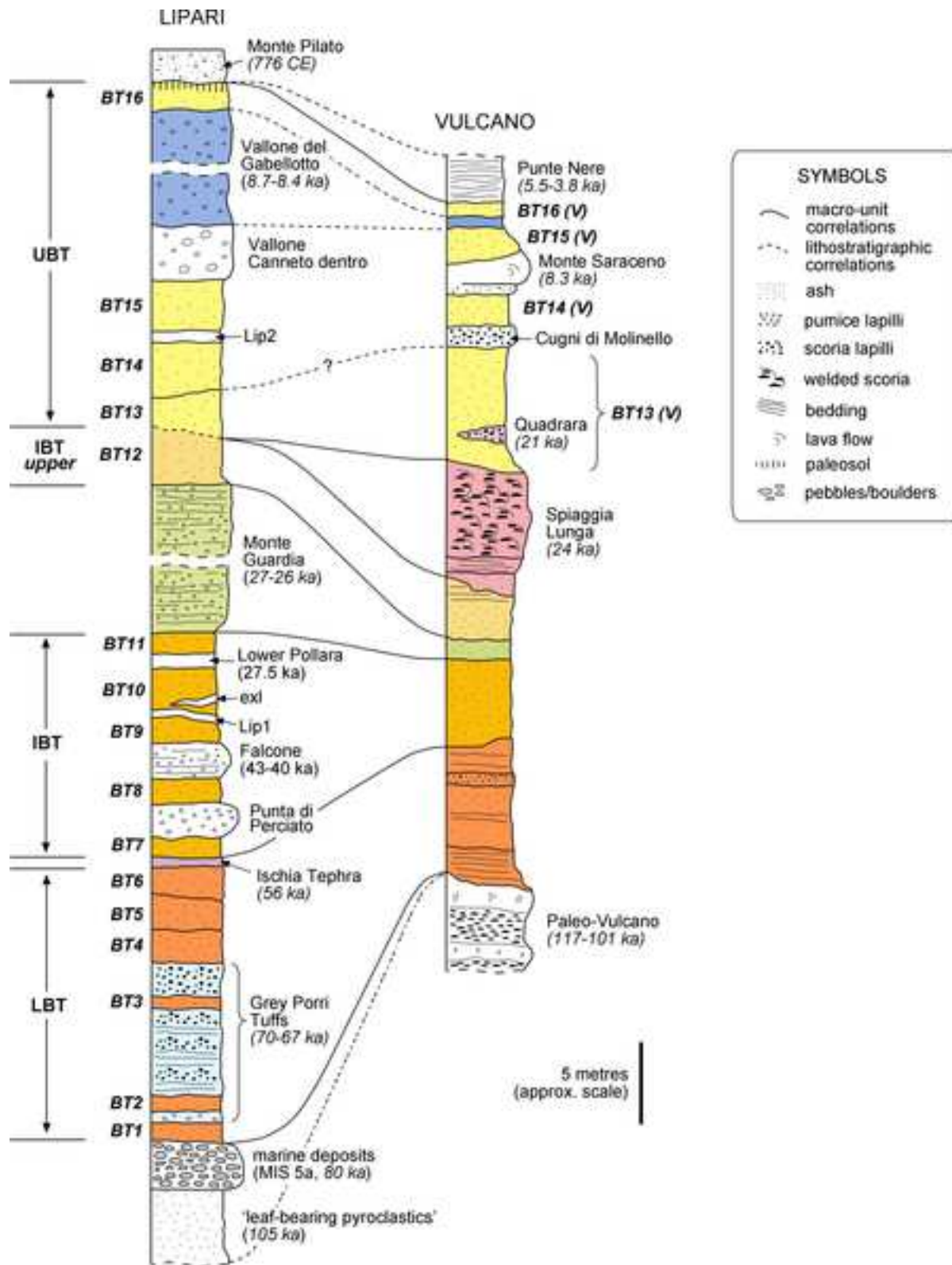


Fig. 2

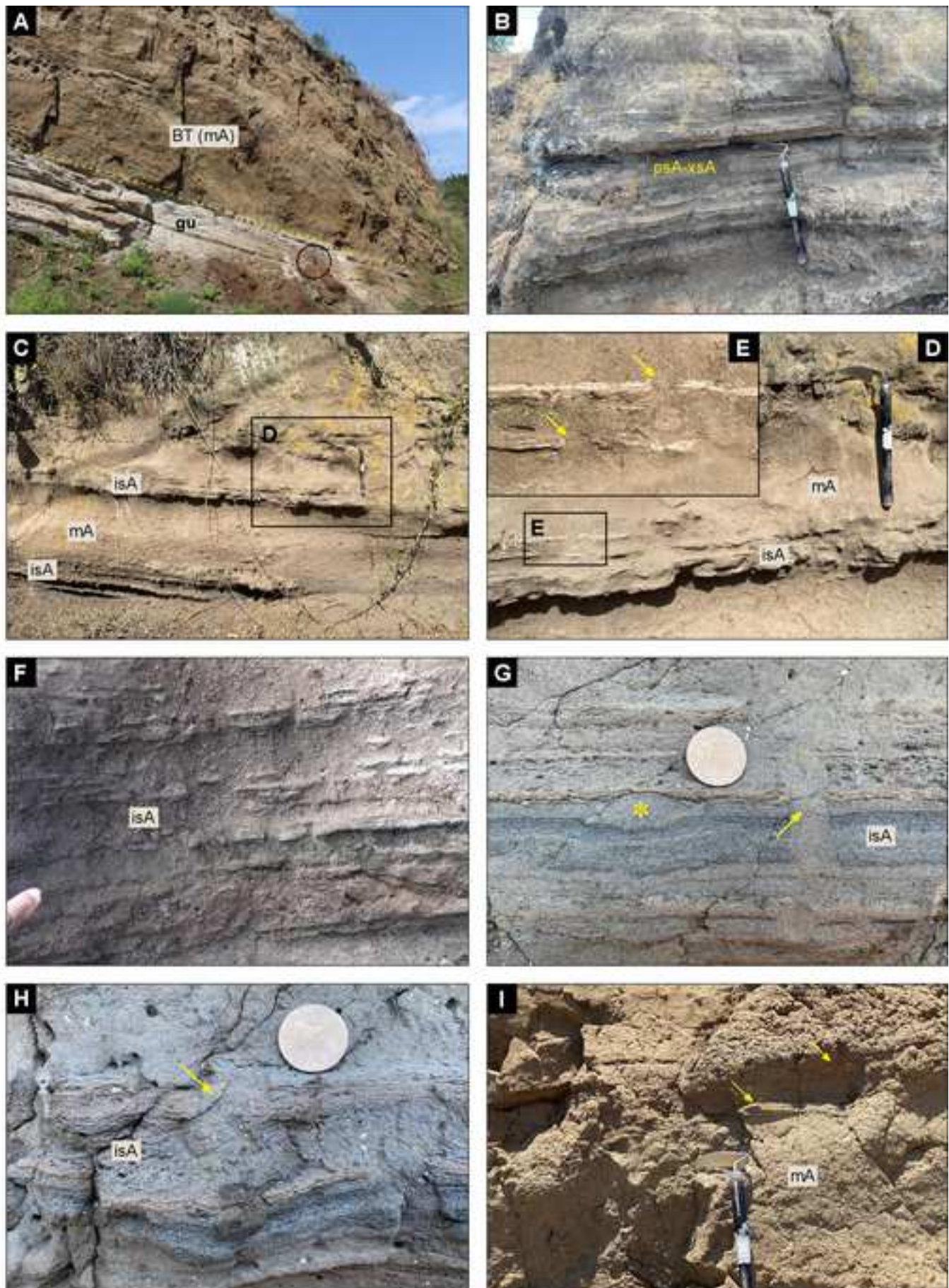


Fig. 3

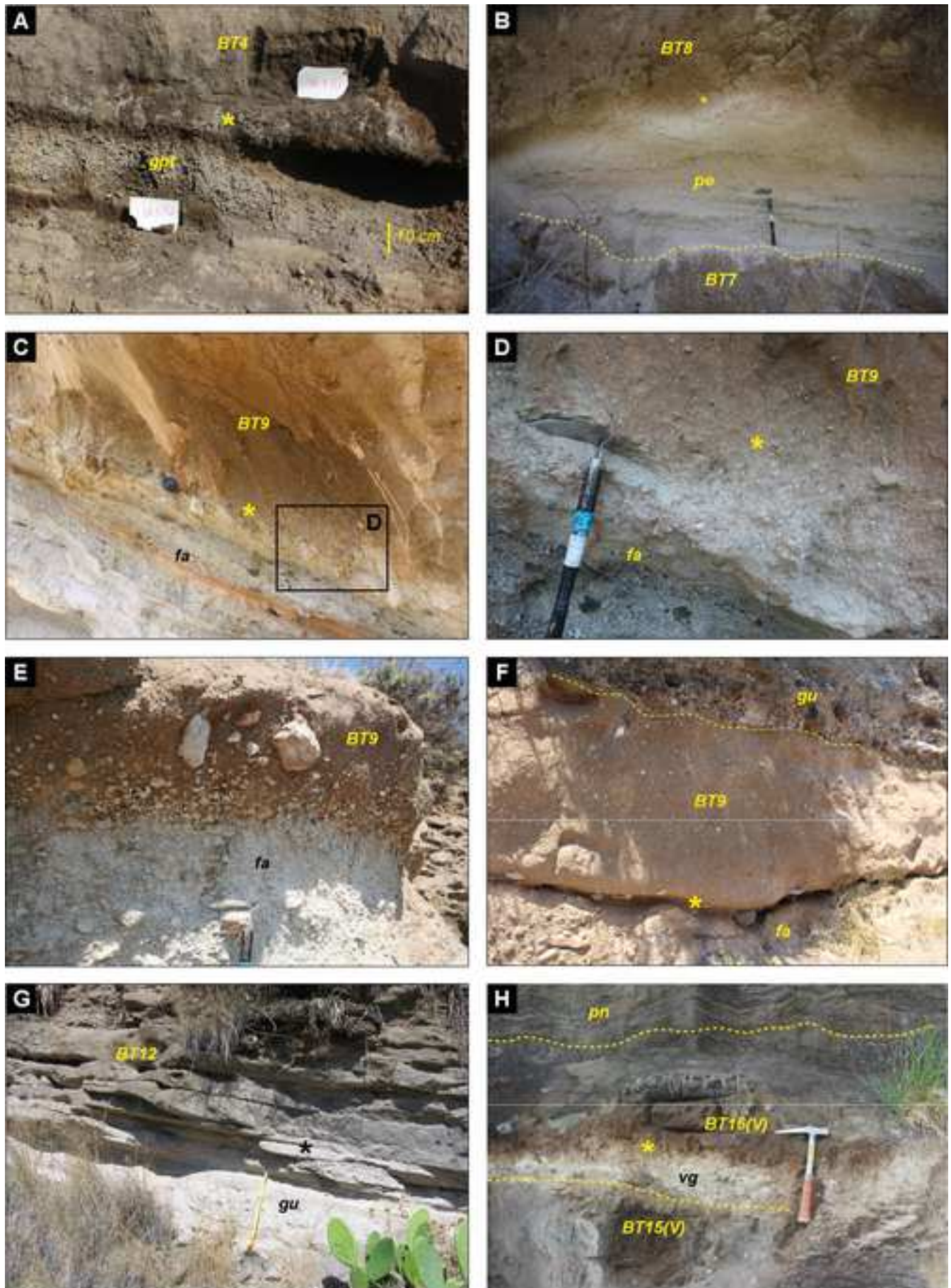


Fig. 4

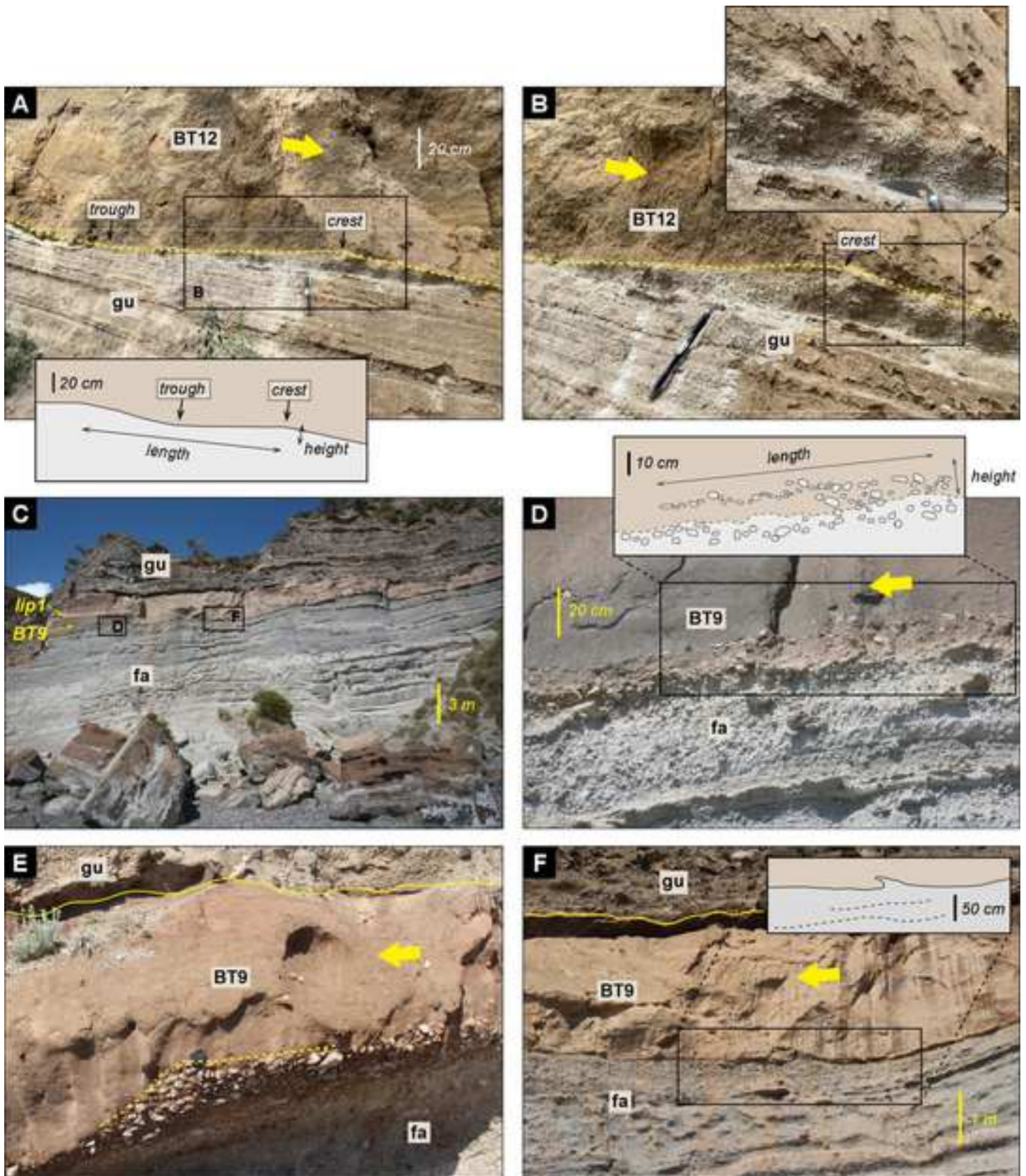


Fig. 5

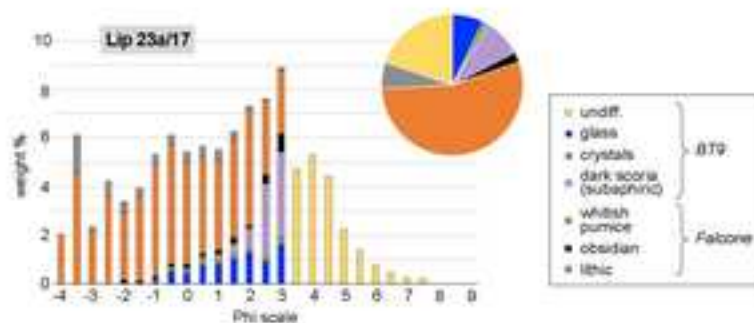
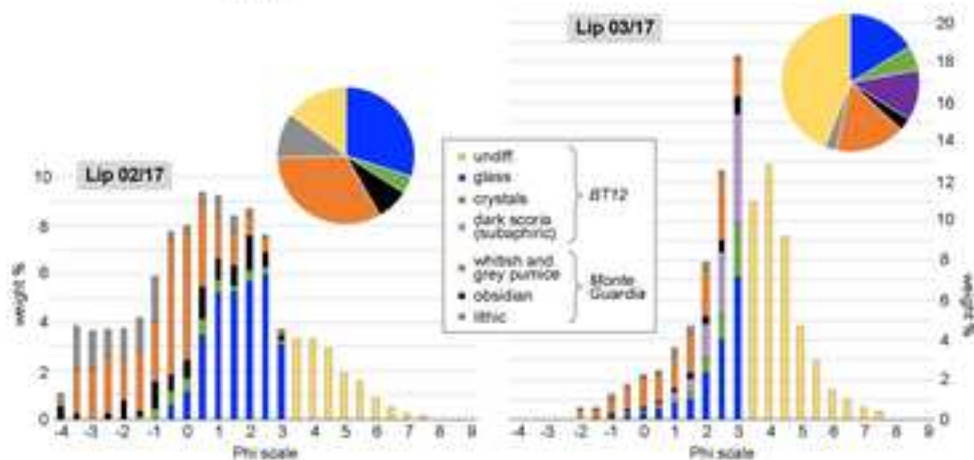
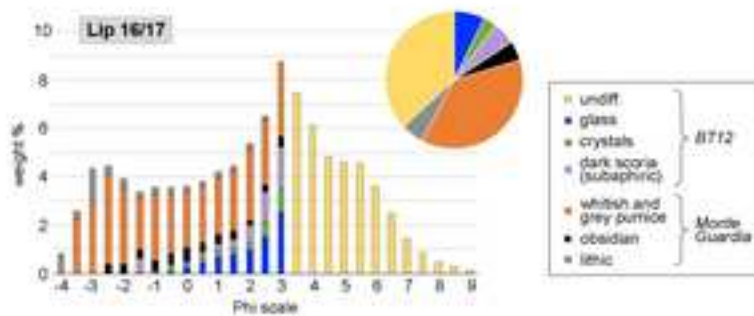
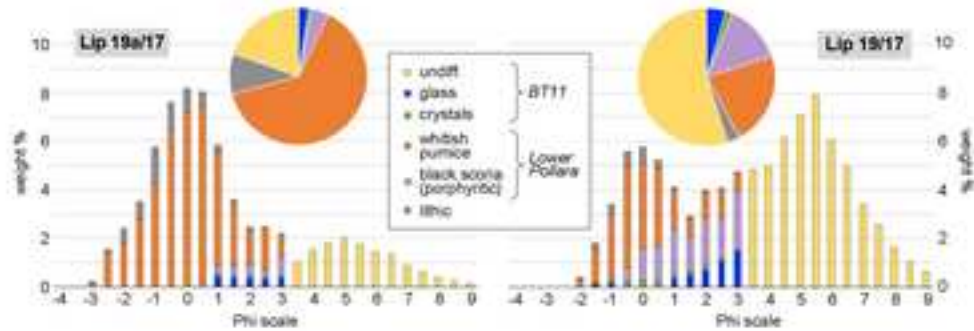
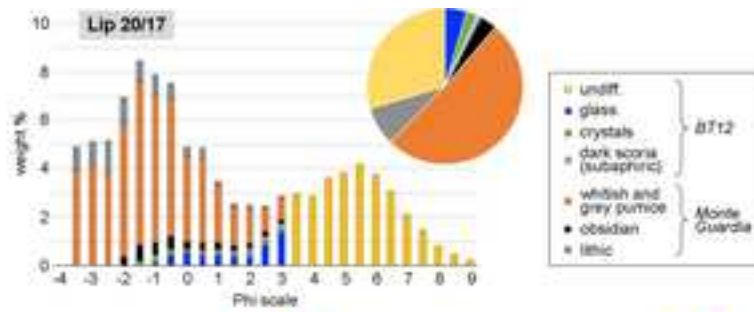


Fig. 6



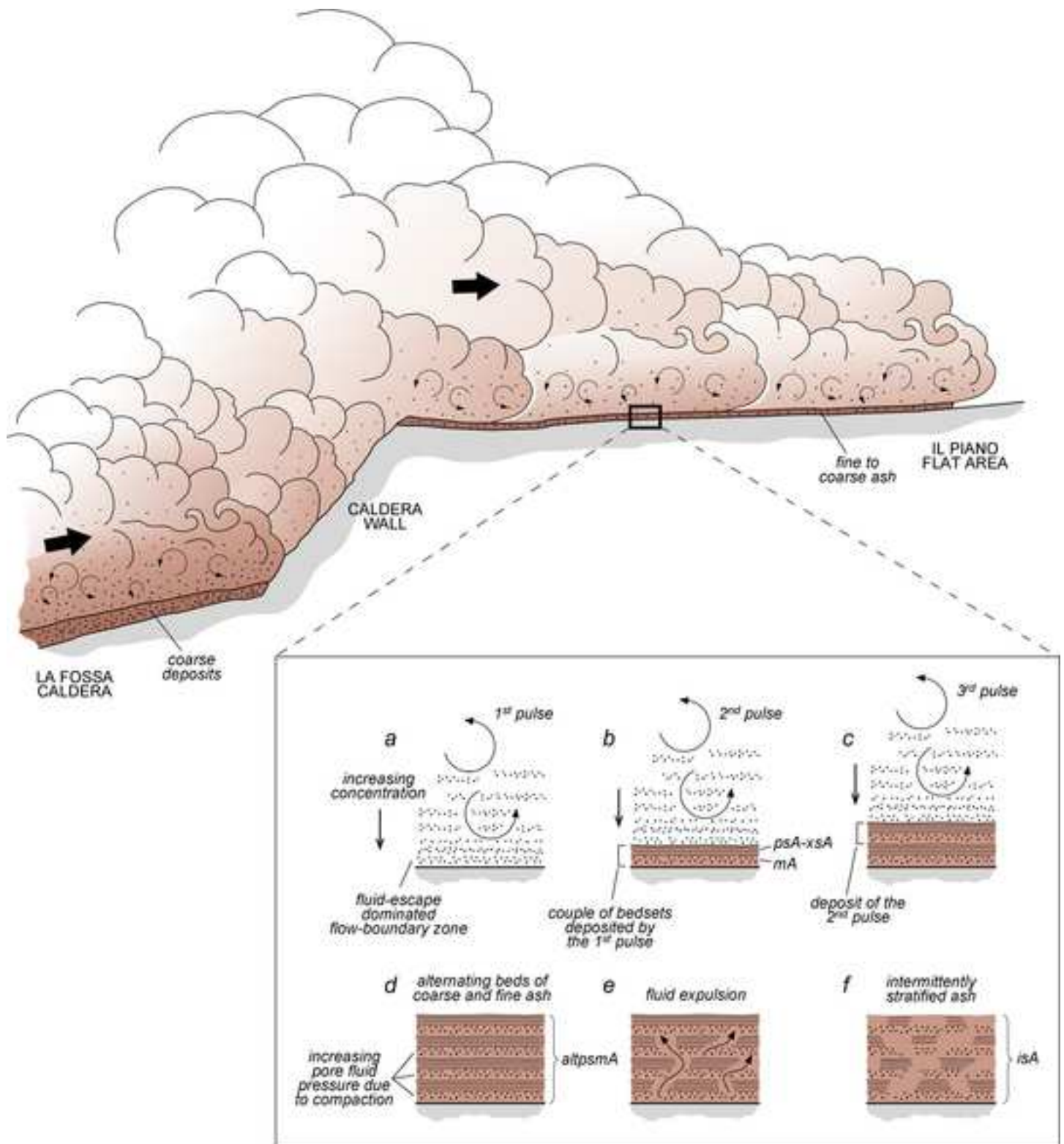


Fig. 8

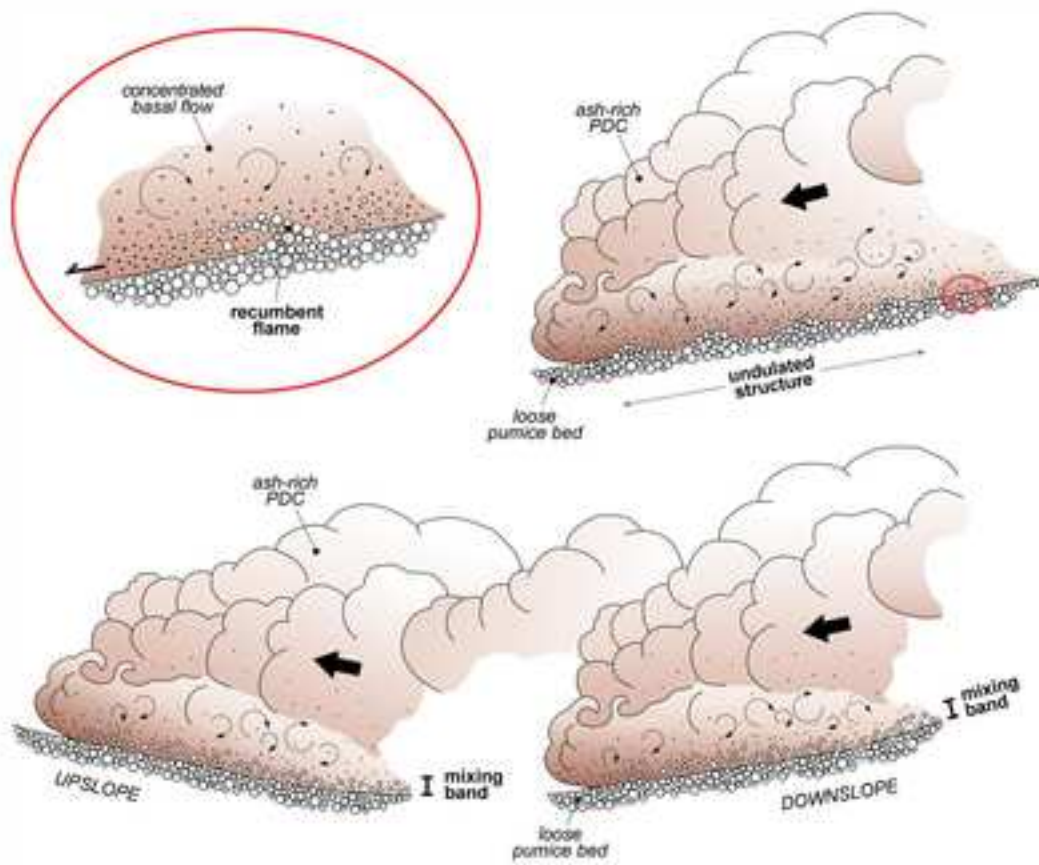


Fig. 9



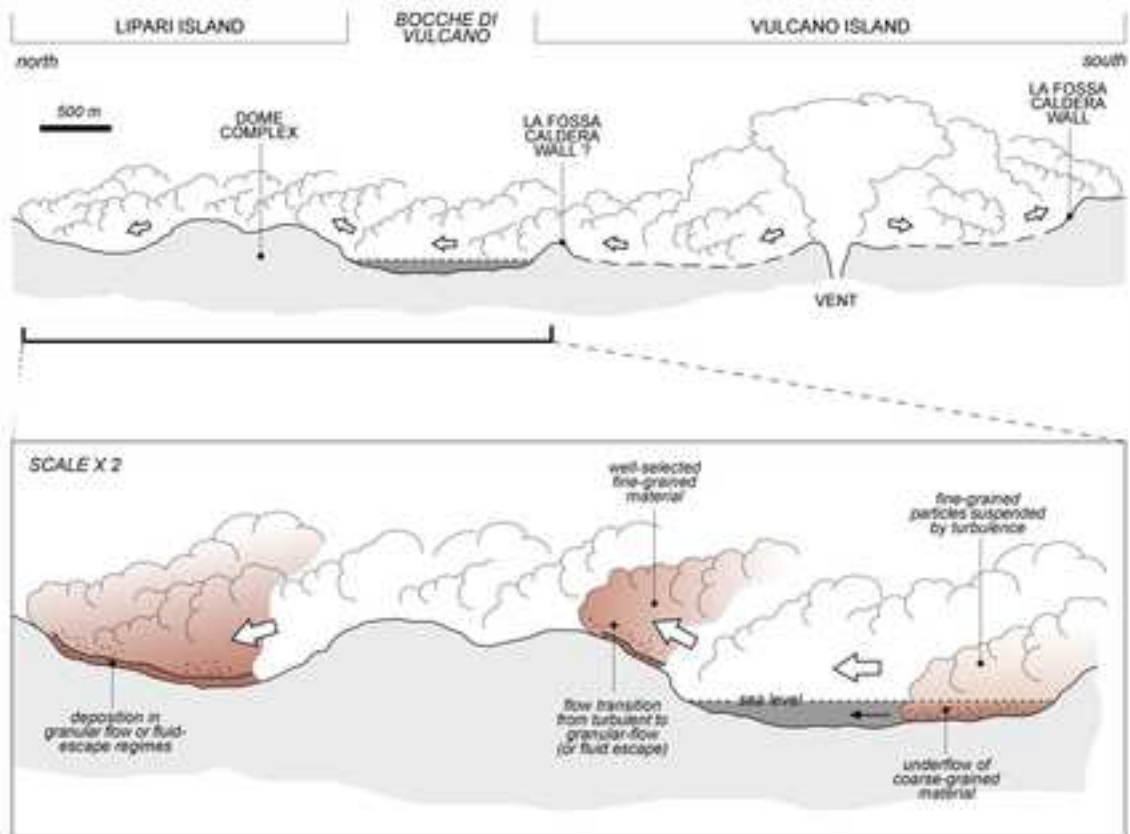


Fig. 10

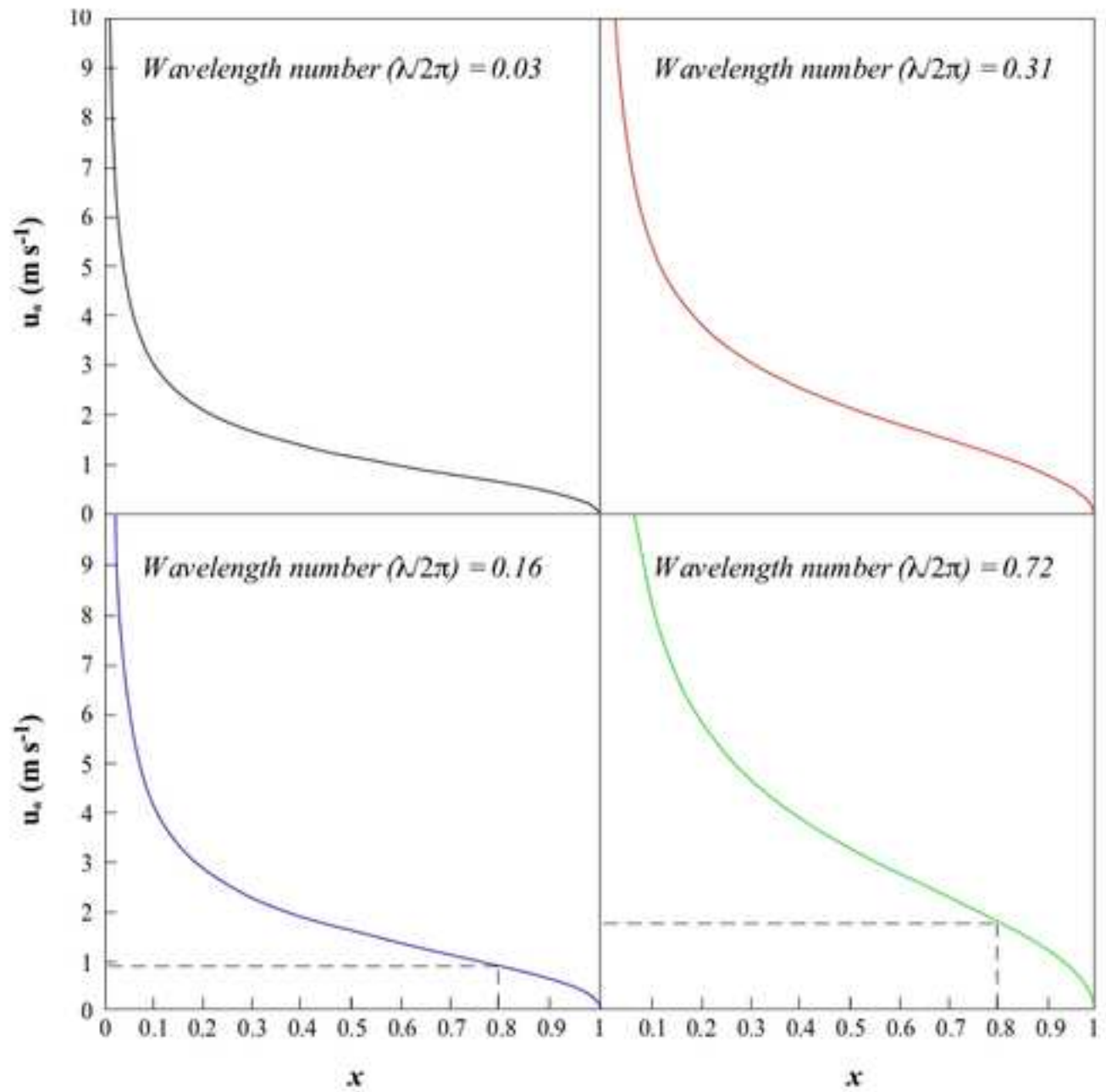


Fig. 11

Table 1 - Selected outcrops, stratigraphy and measurements of the syn-depositional sedimentary structures. The distance from the source area is arbitrarily measured relative to the centre of the La Fossa Caldera. The sample names refer to the BT depositional units selected for chemical analyses. Labels for the sedimentary structures: MB=mixing band; US=undulated structure; FS=recumbent flame structure; RS=rip-up structure. In the column of sedimentary structures the symbol / indicates that there is no direct evidence in the field of mixed lithofacies but the process of clast-embedding is outlined by means of geochemical analyses.

| Island  | Outcrop              | Location                  | Distance (km) | Sedimentary structure | BT dep. unit | Sample name                  | underlying unit                  | Thickness - MB (cm) | Length (cm)           | Height (cm)          |
|---------|----------------------|---------------------------|---------------|-----------------------|--------------|------------------------------|----------------------------------|---------------------|-----------------------|----------------------|
| Lipari  | L0                   | Punta della Crapazza      | 5,5           | /                     | BT10         | Lip15/18, Lip16/18, Lip17/18 | Lip1*                            | /                   |                       |                      |
|         | L1                   | Spiaggia Valle Muria      | 7,7           | MB, US, FS, RS        | BT9          |                              | Falcone                          | ≈30 (max)           | ≈450 (US)<br>≈60 (FS) | ≈20 (US)<br>≈20 (FS) |
|         | L2                   | Valle Muria               | 8.5           | MB                    | BT10         |                              | Lip1                             | ≈5                  |                       |                      |
|         |                      |                           |               | MB                    | BT11         |                              | Lower Pollara                    | 10                  |                       |                      |
|         |                      |                           |               | /                     | BT10         | bt14/16                      | Lip1                             | /                   |                       |                      |
|         |                      |                           |               | MB                    | BT9          |                              | Falcone                          | 25-30               |                       |                      |
|         | L3                   | Chiesa dell'Annunciazione | 9,5           | MB                    | BT8          | bt12/16                      | P. di Perciato                   | ≈10                 |                       |                      |
|         |                      |                           |               | MB                    | BT12         |                              | Monte Guardia                    | ≈25                 |                       |                      |
|         | L4                   | Portinente                | 10            | MB                    | BT12         | bt01/16                      | Monte Guardia                    | n.v.                |                       |                      |
|         | L5                   | Tunnel Canneto            | 10.5          | MB, US                | BT12         |                              | Monte Guardia                    | ≈15                 | ≈250                  | ≈20                  |
|         | L6                   | Vallone Canneto dentro    | 11            | MB                    | BT11         |                              | Lower Pollara Tuffs              | ≈5                  |                       |                      |
|         |                      |                           |               | MB                    | BT9          |                              | Falcone                          | ≈10                 |                       |                      |
|         |                      |                           |               | MB                    | BT7          |                              | Ischia Tephra                    | ≈5                  |                       |                      |
|         |                      |                           |               | MB                    | BT3-BT4      | Lip06/18, Lip07/18           | Grey Porri Tuffs                 | ≈5                  |                       |                      |
|         |                      |                           |               | /                     | BT9-10-11    | Lip45/17                     | Lip1, Falcone or P. del Perciato | /                   |                       |                      |
|         | L7                   | Monterosa                 | 11            | MB                    | BT7          |                              | Ischia Tephra                    | ≈3                  |                       |                      |
|         |                      |                           |               | MB                    | BT4          | bt09/16                      | Grey Porri Tuffs                 | ≈5                  |                       |                      |
|         | L8                   | Vallone dei Lacci         | 12            | MB                    | BT4          | bt09/16                      | Grey Porri Tuffs                 | ≈5                  |                       |                      |
|         | L9                   | Santa Margherita          | 11            | MB                    | BT11         |                              | Lower Pollara Tuffs              | ≈10                 |                       |                      |
|         | L10                  | Madoro                    | 12            | MB                    | BT12         | Lip17/17, Lip18/17           | Monte Guardia                    | ≈25                 |                       |                      |
| MB      |                      |                           |               | BT11                  |              | Lower Pollara Tuffs          | ≈10                              |                     |                       |                      |
| MB      |                      |                           |               | BT9                   |              | Falcone                      | ≈5                               |                     |                       |                      |
| L11     | Vallone Fiume Bianco | 13.5                      | MB            | BT16                  |              | Vallone del Gabellotto       | ≈15                              |                     |                       |                      |
| L12     | Chiesa Vecchia       | 14.5                      | MB            | BT12                  |              | Monte Guardia                | ≈5                               |                     |                       |                      |
|         |                      |                           | MB            | BT11                  |              | Lower Pollara Tuffs          | ≈5                               |                     |                       |                      |
| L13     | Acquacalda           | 16.5                      | MB            | BT16                  |              | Vallone del Gabellotto       | ≈20                              |                     |                       |                      |
|         |                      |                           |               | BT12                  |              | Monte Guardia                | ≈10                              |                     |                       |                      |
| Vulcano | V1                   | Passo del Piano           | 2             | MB                    | BT16 (V)     | bt05/06                      | Vallone del Gabellotto           | ≈10                 |                       |                      |
|         | V2                   | Il Piano                  | 2.5           | MB                    | BT14 (V)     |                              | Cugni di Molinello               | ≈10                 |                       |                      |
|         | V3                   | Il Piano                  | 3             | MB                    | BT14 (V)     |                              | Cugni di Molinello               | ≈10                 |                       |                      |
|         | V4                   | Serra dei Pisani          | 4             | MB                    | BT14 (V)     | bt03/16                      | Cugni di Molinello               | ≈15                 |                       |                      |
|         | V5                   | Gelso                     | 5.7           | MB                    | BT12         | Vul09/17                     | Monte Guardia                    | ≈20                 |                       |                      |
|         | V6                   | Grotta dei Pisani         | 2             | /                     | BT13(V)      |                              | Spiaggia Lunga                   | /                   |                       |                      |

Table 2 - Lithofacies codes, description and interpretation of the lithofacies recognized in the BT investigated in the present work. The first letters of the lithofacies code indicate the general appearance of the deposit (m = massive, ps = planar stratified, xs = cross-stratified, is = intermittently stratified, etc.) and the capital letters indicate the grain size (A = ash, L = lapilli).

| Lithofacies code        | Description  | Interpretation  | Reference        |
|-------------------------|--|---|------------------|
| <b>mA</b>               | Massive, fine to coarse ash, sometimes with scattered pumice and lapilli. Abundant ash aggregates. Geochemically homogeneous. Moderate to poor sorting.  | Gentle settling from a slow-moving, ground-hugging ash cloud. The homogeneous massive appearance suggests deposition from a fine-grained, concentrated flow-boundary zone dominated by fluid escape or granular flow regime. Ash aggregates indicate the presence of steam in the ash cloud or fine ash aggregation driven by electrostatic force during gentle settling of ash from the phoenix cloud of the PDCs.   | Figs. 3A, C-D, I |
| <b>xsA</b>              | Cross-stratified ash, sometimes with laminae. Dune bedded, medium to coarse ash. Moderate to good sorting  | Dune-bedding and internal cross stratification indicate grain by grain deposition from a diluted, turbulent current in which suspension and traction are the main transport mechanisms.   | Fig. 3B          |
| <b>psA</b>              | Planar stratified ash, sometimes with laminae. Moderate to good sorting  | Planar stratification indicate grain by grain deposition from a diluted, turbulent current in which suspension and traction are the main transport mechanisms   | Fig. 3B          |
| <b>altpsmA</b>          | Alternating planar stratified and massive ash. Planar stratified ash sometimes contains laminae. Moderate to good sorting.   | The alternating beds of planar stratified and massive ash testifies for stepwise aggradation of discrete pulses developed within each depositional unit. The massive beds indicate that the flow-boundary zone of each pulse was dominated by granular- or fluid-escape dominated depositional regime. Planar stratified ash beds testify for sedimentation from the waning stage of each pulse, mainly in the traction regime.   |                  |
| <b>isA</b>              | Intermittently stratified ash. Alternation of mm to cm thick massive and stratified beds. The stratified beds are disrupted with distinctive upward deformation and vertical columns of coarse ash at the disruption points. Moderate to good sorting  | Massive beds indicate deposition from a fluid-escape dominated flow boundary zone, whilst the stratified beds indicate deposition from a dilute, turbulent current in which suspension and traction are the main transport mechanisms. The disruption of stratified beds is driven by fluid escape structures related to post depositional dissipation of pore pressure from the underlying massive beds.   | Figs. 3C-H       |
| <i>Shear structures</i> |  |   |                  |
| <b>mixAL</b>            | Mixed ash and lapilli from different units. The ash component is generally homogeneous and forms the matrix of the deposit. The lapilli (and ash) fraction is made by white pumice and dark scoriae eroded from the loose underlying units. Distribution of pumice and scoria may be homogeneous or their abundance decreases regularly upwards within the overlying ash. Massive and generally poorly sorted, with occasional reverse grading of entrained coarse | Mixing of material from different units indicate erosion and incorporation of loose material from the underlying beds into the moving ash flows. The general poor sorting and massive appearance are suggestive of sedimentation from a current in which the rate of supply (Rs) is higher than the rate of deposition (Rd). This induces the rapid development of a highly concentrated zone above the flow boundary, dominated by fluid escape or granular flow regimes. The moving flow exerted shear stress over the loose substratum, causing entrapment of clasts into the flow body. The occasional reverse grading of entrained coarse clasts reveals dispersive pressure | Figs. 4A-H       |

|             |  |  |            |
|-------------|--|--|------------|
|             | clasts.  | processes induced by grain-grain collision in a high-concentration zone at the base of the current.  |            |
| <b>ucAL</b> | Undulated contact between ash and underlying lapilli and ash beds. The contact between the ash beds and the underlying units is represented by a transitional mixing band with wavelength of decimeters to meters. The upper part of the undulated mixed material shows imbrication of coarser clasts. | The undulated contact between ash and underlying lapilli and ash beds indicates shear exerted by the overriding flows to the loose underlying units, which induces remobilization of its upper part producing imbrication of coarse clasts and formation of waves with variable wavelength. These structures indicate high shear stress exerted by the ash flows to the substratum. Imbrication of coarse clasts testifies for the occurrence of traction carpet processes with remobilisation of the sheared material in a frictional regime. | Figs. 5A-C |
| <b>rfAL</b> | Recumbent flame structures of lapilli from the underlying beds within the ash units. The upper part of the underlying lapilli bed is ripped up and bended downflow to form an alignment of lapilli within the ash deposit.   | Recumbent flame structures indicate high shear exerted by the overriding ash flows over the underlying lapilli beds, which produce incorporation of lapilli that are aligned downflow for a distance up to some meters.  | Figs. 5D-E |
| <b>ruAL</b> | Rip up lapilli from the underlying beds into the ash units. Small hook-like structures visible at the contact between ash and lapilli beds. The main part of the contact is almost planar.   | Small hook-like structures indicate moderate shear exerted from the overriding ash flow, which is not able to significantly displace the upper part of the underlying lapilli bed.   | Fig. 5F    |

Table 3. Grain size statistical parameters of Folk and Ward (1957) for the different sub-populations recognised in the samples from the base of some BT depositional units: BT=Brown Tuffs; mg=Monte guardia unit; lpt=Lower Pollara Tuffs; fa=Falcone unit. The parameters by Folk and Ward (1957) were calculated by means of the GRADISTAT program (Blott and Pye, 2001). The Sauter mean diameter (Sauter 1926) of the different BT sub-populations is estimated using the method of Breard et al. (2019).

| Sample        |               | LIP02/17 |       | LIP03/17 |       | LIP16/17 |       | LIP20/17 |       | LIP19/17 |      | LIP19a/17 |       | LIP23a/17 |       |
|---------------|---------------|----------|-------|----------|-------|----------|-------|----------|-------|----------|------|-----------|-------|-----------|-------|
|               |               | BT       | mg    | BT       | mg    | BT       | mg    | BT       | mg    | BT       | lpt  | BT        | lpt   | BT        | fa    |
| Median        | ( $M\phi$ )   | 1,98     | -0,94 | 3,22     | 1,34  | 3,74     | -0,76 | 4,70     | -1,45 | 4,97     | 0,19 | 4,73      | -0,22 | 3,13      | -0,59 |
| Mean          | ( $\bar{x}$ ) | 2,18     | -1,09 | 3,25     | 1,05  | 3,80     | -0,66 | 4,39     | -1,29 | 4,84     | 0,40 | 4,62      | -0,18 | 3,04      | -0,64 |
| Sorting       | (s)           | 1,71     | 1,79  | 1,29     | 1,35  | 1,83     | 2,07  | 2,10     | 1,60  | 1,78     | 1,32 | 1,79      | 1,29  | 1,53      | 2,04  |
| Skewness      | ( $Sk$ )      | 0,19     | -0,07 | -0,08    | -0,65 | -0,29    | 0,10  | -0,72    | 0,47  | -0,63    | 0,26 | -0,25     | 0,19  | -0,28     | -0,08 |
| Kurtosis      | ( $K$ )       | 0,93     | 0,89  | 4,01     | 2,45  | 3,40     | 1,75  | 3,31     | 2,65  | 4,17     | 2,07 | 2,69      | 2,77  | 3,25      | 1,89  |
| Sauter number | ( $D_{32}$ )  | 0,25     |       | 0,11     |       | 0,08     |       | 0,04     |       | 0,03     |      | 0,04      |       | 0,11      |       |